SEMMELWEIS EGYETEM

DOKTORI ISKOLA

Ph.D. értekezések

3216.

CHRIST CAROLIN

Celluláris és molekuláris élettan

című program

Programvezető: Dr. Várnai Péter, egyetemi tanár, az MTA doktora

Témavezető: Dr. Jakus Zoltán Péter, egyetemi docens

A New Approach to Visualize and Characterize the Lymphatic Vasculature in Atherosclerosis

PhD Thesis

Carolin Christ

Doctoral School of Molecular Medicine

Semmelweis University

Supervisor:

Zoltán Jakus MD, PhD

Official reviewers:

Marianna Török, PhD, Péter Engelmann, PhD

Head of the Complex Examination Committee:

Zoltán Ungvári MD, PhD

Members of the Complex Examination Committee:

László Hiripi, PhD, Zoltán Wiener, PhD

Budapest

2025

Table of Contents

List of Abbreviations 4

1. Introduction 6

1.1 The Lymphatic System 6

1.1.1 The Lymphatic System and its Traditional Functions 6

..... 7

1.1.2 Development of the Lymphatic Vasculature 7

1.1.3 Organ-Specific Functions of Lymphatic Vessels 8

1.2 The Lymphatic Vasculature in Atherosclerosis 10

1.2.1 Atherosclerosis 10

1.2.2 Lymphatic Vasculature and Reverse Cholesterol Transport 12

1.2.3 Role of Lymphatic Vessels in the Development and Progress of Atherosclerosis 13

1.3 Visualization of the Lymphatic System 13

1.3.1 Traditional Visualization Techniques of Lymphatic Vasculature 13

1.3.2 Tissue-Clearing Techniques 14

2. Objectives 16

3. Materials and Methods 17

3.1 Mouse Models 17

3.2 Special Diet for Atherosclerosis Development 17

3.3 Body Weight and Serum Cholesterol Measurements 18

3.4 Paraffin-Based Histology and H/E staining 18

3.5 Masson-Trichrome Staining of Paraffin Sections 18

3.6 Alizarin Red S Staining of Paraffin Sections 19

3.7 Immunostaining of Sections 19
3.8 Detection and Imaging of Native Fluorescence 19
3.9 In Situ Brightfield Images of Aortas 19
3.10 Whole-Mount Oil Red O Staining of Aortas 20
3.11 Whole-Mount Alizarin Red S Staining of Aortas 20
3.12 Tissue Clearing and Whole-Mount Immunostaining 20
3.12.1 Cardiac Perfusion and Tissue Collection 20
3.12.2 Decolorization and Delipidation 21
3.12.3 Whole-Mount Immunostaining 21
3.12.4 Adjustment of the Refraction Indices (RI-Adjustment) 22
3.13 Microscopic Imaging and Processing 22
3.14 Quantification of Cross-Sectional Atherosclerotic Plaque Area 22
3.15 Quantification of Fibrosis in Cross-Sections of the Aorta 22
3.16 Manual Quantification of Lymphatic Structures in Paraffin Sections 22
3.17 Quantification of Lymphatic Structures in Tissue-Cleared Samples with AngioTool 23
3.18 Data Representation and Statistical Analysis 23
4. Results 24
4.1 Visualization of Organ-Specific Lymphatic Growth 24
4.1.1 Visualization of Lymphatics with Traditional Methods 24
4.1.2 Our Optimized Tissue-Clearing Approach 25
4.1.3 Visualization of Lymphatic Vessels with Our Optimized Tissue-Clearing Protocol 26
4.1.4 Quantification of Lymphatic Structures with AngioTool 29
4.1.5 Morphological Changes of the Organ-Specific Lymphatic Vasculature of *Flt4*$^{kd/+}$ Mice 31

4.1.6 Quantification of Morphological Changes of the Lymphatic Vasculature of *Flt4*$^{kd/+}$ mice 33

4.2 Characterization of the Lymphatic Vasculature in Atherosclerosis 36

4.2.1 Characterization of the Lymphatic Vasculature in Different Segments of the Great Vessels 36

4.2.2 Western Diet Leads to Elevated Body Weight and Serum Lipids in Male and Female Mice 38

4.2.3 Female Mice Tend to Develop Larger Plaques Than Males When Fed a Western Diet 39

4.2.4 Female Mice on a Western Diet Develop Significantly Larger Plaque Calcifications Than Males 41

4.2.5 Lymphatic Count and Total Lymphatic Lumen in Arterial Walls of Atherosclerotic Mice Remain Unchanged 43

4.2.6 Sex-Dependent Lymphatic Vessel Dilation in the Abdominal Aorta of Female Mice on a Western Diet 45

4.2.7 No Significant Changes in Lymphatic Vessels in Other Organs of *Ldlr*$^{-/-}$ Mice on a Western Diet 47

4.2.8 Enhanced Peripheral Lymphatic Function in Females on a Western Diet 48

5. Discussion 50

6. Conclusion 56

7. Summary 57

8. References 58

9. Bibliography of the candidate's publications 72

9.1 Publications included in this dissertation 72

9.2 Publications not included in this dissertation 72

10. Acknowledgments 73

List of Abbreviations

ApoE	Apolipoprotein E
ADAMTS3	A disintegrin and metallopeptidase with thrombospondin motifs 3
CCBE1	Collagen and calcium-binding epidermal growth factor domain-containing protein 1
CUBIC	Clear, unobstructed brain/body imaging cocktails and computational analysis
CV	Cardinal vein
DAPI	4’,6-diamidino-2-phenylindole
E12.5	Embryonic day 12.5
E9.5	Embryonic day 9.5
EC	Endothelial cell
FH	Familial hypercholesterolemia
FLT4	Fms-related tyrosine kinase 4
GFP	Green fluorescent protein
HDL	High-density lipoprotein
H/E	Haematoxylin and Eosin
H_2O	Water
ICAM-1	Intercellular adhesion molecule-1
IU	International units
JLS	Jugular lymph sac
kDa	Kilodalton
KOH	Potassium Hydroxide
LDL	Low-density lipoprotein
Ldlr	LDL-Receptor
LEC	Lymphatic endothelial cell
LV	Lymphatic vessel
LYVE1	Lymphatic vessel endothelial hyaluronan receptor 1
M-CSF	Macrophage colony-stimulating factor
oxLDL	Oxidized LDL
PBS	Phosphate-buffered saline
PFA	Paraformaldehyde

Prox1	Prospero-related homeobox 1
RCT	Reverse cholesterol transport
RhD	Rhodamine-dextran
RI	Refractive Index
ROS	Reactive oxygen species
Rpm	Revolutions per minute
SEM	Standard error of mean
VCAM-1	Vascular cell adhesion molecule-1
VEGF-C	Vascular endothelial growth factor-C
VEGFR-3	Vascular endothelial growth factor receptor-3
vWF	Von Willebrand Factor
WOBLI	Whole organ blood and lymphatic vessel imaging
αSMA	Alpha smooth muscle actin

1. Introduction

1.1 The Lymphatic System

1.1.1 The Lymphatic System and its Traditional Functions

The lymphatic system is an open and low pressure vascular system. It consists of lymphatic vessels, lymph nodes and other organs such as spleen and tonsils.

Traditional functions of the lymphatic system have been known for centuries and include the uptake of dietary lipids, immune cell trafficking and transport of interstitial fluid and macromolecules [1]. Lymphatic vessels play a pivotal role in the initial immune response by serving as the main transport system for antigens and antigen-presenting cells from the periphery to lymph nodes [2]. Fluids, molecules and cells from peripheral tissues are absorbed via 30 to 80 µm wide highly permeable thin-walled and blindly ending lymphatic capillaries. These capillaries are non-contracting vessels consisting of a single layer of lymphatic endothelial cells (LECs) with button-like junctions that allow fluid, immune cells and macromolecules to enter the lymphatic circulation system where these components become the so-called lymph, a milky fluid consisting of interstitial fluid, cells, macromolecules and proteins (**Figure 1**) [3]. In the past it was believed that venous capillaries are uptaking most of the capillary ultrafiltrate and plasma proteins, but new evidence showed that a lot of interstitial fluid is uptaken by lymphatics, highlighting the importance in maintaining fluid homeostasis [4]. Several liters of extravasated plasma are absorbed and transported by the lymphatics per day. Absorption of fluid depends on a pressure gradient from the interstitium into the lymphatic capillaries. These capillaries are connected by button-like junctions and sense increased interstitial pressure via specialized anchoring filaments. This leads to the opening of special valves that allow entrance of fluid and cells. Lymphatic capillaries drain into pre-collecting and collecting lymphatics in which LECs are connected by impermeable tight zipper-like junctions. Collecting lymphatic vessels are covered by a smooth muscle layer that contracts regularly and helps with the transport of lymph against a pressure gradient, although extrinsic forces such as skeletal and visceral smooth muscle contractions support lymph flow [5] . Lymphatic valves in collecting lymphatics divide collecting vessels into small segments, the lymphangions. Lymphangions act as pumping units and pump lymph with regular contractions through collecting lymphatic vessels to the lymph nodes to be screened for antigens that mediate immune responses. Lymph is transported through the

thoracic and right lymphatic duct where it enters the venous system via lymphovenous valves [6,7].

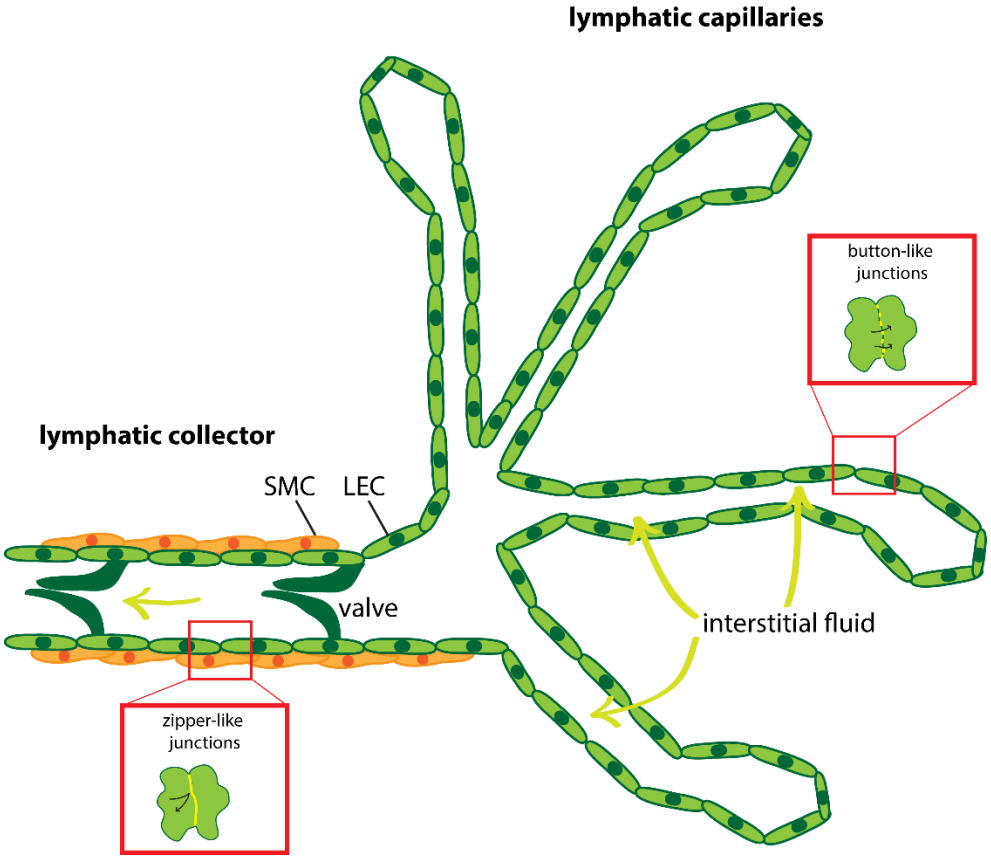

Figure 1: Structure of lymphatic collectors and capillaries. Blindly ending lymphatic capillaries connected by button-like junctions between the lymphatic endothelial cells (LECs) take up interstitial fluid and macromolecules from the interstitial space. Fluid is transported by contracting lymphatic collectors with the help of smooth muscle cells (SMC) and valves that ensure unidirectional lymph flow (own work, unpublished).

1.1.2 Development of the Lymphatic Vasculature

Nowadays, it is mainly accepted that lymphatic vessels have a "venous origin". Around embryonic day 9.5 (E9.5), a subset of endothelial cells (ECs) of the cardinal vein (CV) start to express *Prox1* (*prospero-related homeobox 1*), an important factor that determines lymphatic endothelial cell fate [8-11]. These ECs then differentiate into progenitor LECs and form the jugular lymph sac (JLS) from which LECs are sprouting in order to form the first primitive lymphatic vessels [12-14].

Around E12.5, the developing lymphatic endothelium expresses vascular endothelial growth factor receptor-3 (VEGFR-3 or *Flt4*), the receptor for vascular endothelial growth factor-C (VEGF-C) [15,16]. VEGF-C is translated in its inactive form and has to be

cleaved by the metalloprotease ADAMTS3 that is activated by CCBE1 [17-19]. VEGFR-3 serves as a mediator for lymphatic and blood vessels during development but its postnatal expression is restricted to the lymphatic vasculature [15]. Mutations of *Flt4* have been shown to lead to lymphatic dysfunction, and to the development of primary or hereditary lymphedema, indicating the importance of the VEGFC-VEGFR3 signaling axis [20,21]. The $Flt4^{kd/+}$ mouse strain carries a mutated *Flt4* allele that leads to the inactivation of the tyrosine kinase activity of VEGFR-3 in mice, causing chylous ascites, enlarged lymphatics in the intestinal tissue, missing lymphatic vessels in the skin and swollen feet, all symptoms of lymphatic dysfunction [22]. Despite the fact that the $Flt4^{kd/+}$ mouse strain shows symptoms of lymphatic dysfunction in the skin, detailed studies of the lymphatic vessels of other organs have not been carried out to date.

Lymphangiogenesis is also promoted by signaling via the hyaluronan receptor LYVE1, expressed almost exclusively by LECs. [23,24]. Lymphatic vessels are responsible for hyaluronan transport from tissues such as skin and intestine, but very little is known about the exact role of lymphatic vessels in the transport of hyaluronan [25]. Since LYVE1 is almost exclusively expressed on lymph vessels and is absent from blood vessels, it is widely used as a lymphatic vessel marker and has helped to investigate the structure and function of the lymphatic system since its discovery in 1999. LECs of lymphatic capillaries express higher levels of LYVE1 than LECs of collecting lymphatic vessels [3]. Interestingly, mice deficient in LYVE1 (no functional gene product) show normal lymphatic development, whereas LYVE1-null mice (no gene product) show morphologically and functionally altered lymphatic capillaries [26,27]. LYVE1 is also expressed in the sinusoid endothelium of liver and spleen and activated macrophages [28]. LYVE1 is therefore a great marker of LECs, but not essential for lymphatic development.

1.1.3 Organ-Specific Functions of Lymphatic Vessels

Lymphatics can be found in nearly every organ of the mammalian body. Besides the traditional functions, lymphatic vessels have been found to have important organ-specific roles, not only in the maintenance of healthy organ function, but also during development and tissue regeneration. Organ-specific lymphatic vessels show strong heterogeneity and plasticity and adapt to the local environments via specialized functional properties. Lymphatic dysfunction is associated with the development and progression of various

pathologies such as lymphedema, inflammatory diseases, obesity, tumor growth and other metabolic diseases [29-32].

Skin, the first line of defense against pathogens, contains an extensive network of lymphatic capillaries in the dermis. Impairment of dermal lymphatic function leads to lymphedema, hyperpigmentation, keratosis, and papillomatosis, showing that the lymphatic vasculature is important for normal skin homeostasis [33]. Lymphatics also play an important role during skin regeneration by interacting dynamically with the hair follicle stem cell niche [34].

The function of intestinal lymphatic vessels is the uptake and transport of dietary lipids, usually in the form of chylomicrons with a size of 200-1000 nm. Intestinal lymphatic vessels form the lacteal, a single lymphatic vessel in the center of each intestinal villus. Lacteals take up chylomicrons and fluid and transport them to the collecting lymphatic vessels located in the mesenteries. Besides lacteals, the intestinal lymphatic system also consists of the lymphatic vascular plexus in the intestinal muscular layer that drains independently of the lacteals into the collecting lymphatic vessels of the mesentery.

Impaired intestinal lymphatic function can worsen intestinal inflammation and symptoms in experimental models of colitis and plays a role in the pathogenesis of Crohn's Disease [35-37].

The pulmonary lymphatic system is an extensive network of vascular structures essential for immunity and the body's defense against pathogenic material. Lung lymphatics run parallel to the major airways, bronchioles and close to the intralobular arterioles and small veins. Lymph from the surface of the lungs is drained via a network of subpleural lymphatics. Lymphatics have been shown to be altered in COPD and lymphatic dysfunction caused by cigarette smoke could lead to the development of lung emphysema [38].

Lymphatic vessels in the embryonic lung are especially important because they are preparing the developing lung for inflation after birth and mice with lymphatic dysfunction die shortly after birth [39,40].

Lymphatic vessels also play a role in inflammation of various organs. Studies have shown that lymphatic vessels play a role in both acute inflammatory reactions and chronic inflammatory diseases. Inflammation leads to lymphangiogenesis, the growth of new lymphatic vessels and to lymphatic hyperplasia, the dilation of lymphatic vessels. A role

of the lymphatic vasculature has been studied in arthritis, inflammatory bowel disease, dermatitis and atherosclerosis [41-44]. With lymphatics being involved in numerous organs, it is important to define their organ-specific functions in more detail.

1.2 The Lymphatic Vasculature in Atherosclerosis

1.2.1 Atherosclerosis

Atherosclerosis is a chronic inflammatory disease of medium and large sized arteries and is characterized by endothelial damage and influx of low-density lipoprotein (LDL) into the intimal space of the arterial wall. Cigarette smoke, diabetes and elevated blood sugar levels, hypercholesterolemia, aging and a high-fat cholesterol-rich Western diet are the major risk factors of developing atherosclerosis [45-48]. Accumulated LDL undergoes oxidation in the arterial wall, propagating an immune reaction including recruitment, homing, migration and differentiation of monocytes. Endothelial injury leads to the upregulation of cell adhesion molecules such as vascular cell adhesion molecule-1 (VCAM-1), selectin and intercellular adhesion molecule-1 (ICAM-1) which enable monocytes to attach to the endothelium and enter the arterial wall [49]. Monocytes differentiate into macrophages by macrophage colony-stimulating factor (M-CSF) when they enter the endothelium, a crucial factor for atherosclerosis development. The newly differentiated macrophages phagocyte oxidized LDL via scavenger receptors that are expressed on the cell surface, becoming so-called foam cells that release pro-inflammatory or pro-atherogenic cytokines, enzymes and reactive oxygen species (ROS) [50-52]. This early phase of the atherosclerotic plaque development is called the fatty streak (**Figure 2**). In this phase, efferocytosis, the removal of apoptotic cells is still possible and prevents the formation of a necrotic core. When macrophage foam cells undergo cell death so quickly, that efferocytosis is not possible anymore, the necrotic core of the atherosclerotic plaque is starting to grow. Smooth muscle cells migrate from the arterial wall to form a fibrous cap encapsulating the necrotic core. Thin, fibrous caps are an indication for a vulnerable plaque that can rupture easily. Vascular calcifications can occur if smooth muscle cells are undergoing apoptosis, micro-calcifications can be caused by matrix vesicles released by macrophages or apoptosis of macrophages [53]. Calcification can start in the necrotic core, where apoptosis of foam cells takes place. Atherosclerotic plaques with calcifications consisting of calcified vesicles, the precursors

of micro-calcifications, are more susceptible to rupture due to increased stress [54]. A strong correlation between calcification and lesion size can be observed.

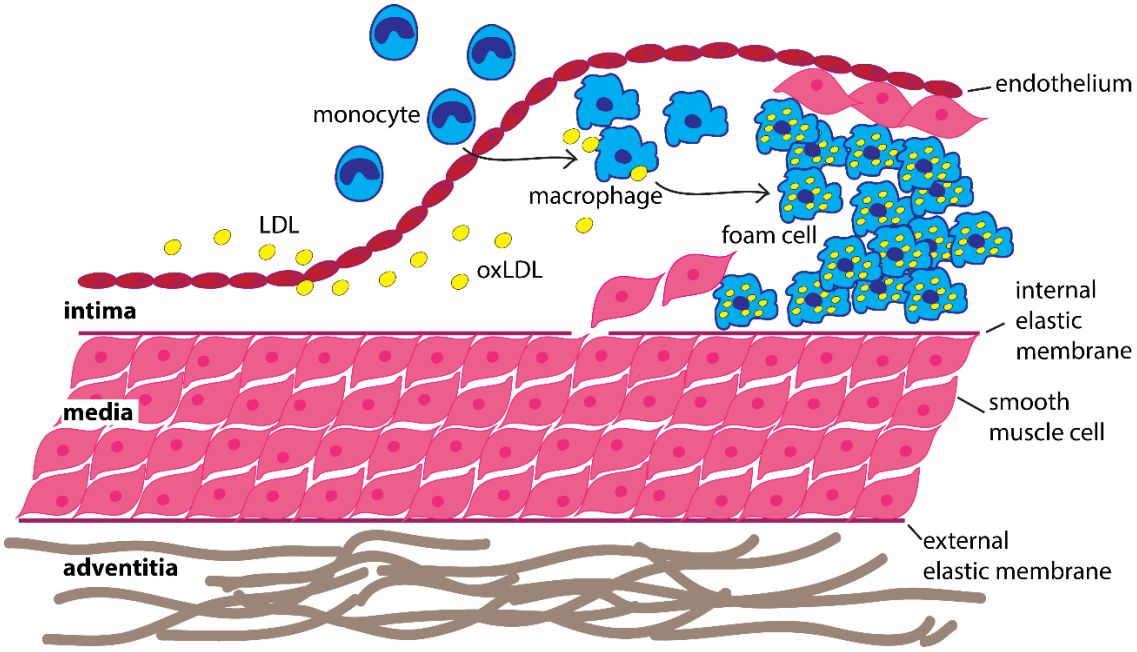

Figure 2: Pathogenesis of atherosclerosis. The build-up of a fatty streak, the early atherosclerotic plaque, begins with the influx of LDL through the damaged endothelium into the intima of the arterial wall. LDL undergoes oxidation and attracts monocytes that trespass the endothelium and differentiate into macrophages. Macrophages engulf the oxidized LDL and become so-called foam cells that make up the majority of the fatty streak (own work, unpublished).

The plaque formation progresses over decades as the atherosclerotic plaque size is continually increasing until the plaque cannot withstand the increase in pressure of the blood flow and ruptures. The rupture leads to exposure of deep arterial wall components, leading to platelet activation, thrombosis and disturbed blood flow and oxygen transport to vital organs and to further cardiovascular events such as myocardial infarction and stroke. Atherosclerosis is one of the major health burdens and the underlying cause of death of nearly half the population in a westernized society [55]. Therefore, stabilization of plaques and suppression of atherosclerotic progression is important to prevent acute coronary syndromes and stroke.

Mouse models used in atherosclerotic research lack factors important for the cholesterol transport, such as the *ApoE*$^{-/-}$ mouse model, lacking Apolipoprotein E (APOE) or the *Ldlr*$^{-/-}$mouse model, lacking the LDL-Receptor (LDLR). Both mouse models are suffering

from severe hyperlipidemia and develop atherosclerotic plaques, especially when fed a cholesterol-rich Western diet [56-62]. The absence of LDLR leads to an accumulation of LDL in plasma resulting in an extensive elevation of total plasma cholesterol levels.

Mice without modifications of the lipid metabolism are relatively resistant to elevated plasma cholesterol levels and do not develop atherosclerosis under normal conditions [58,59]. Researchers suggested that LDL receptors are largely responsible for the resistance of wild type mice to atherosclerosis, since no atherosclerotic related changes were seen in wild type mice that were fed a high-fat diet [63]. Experiments with *ApoE*$^{-/-}$ mice have shown that it contains the entire spectrum of lesions usually observed in atherosclerosis and the atherosclerotic lesions are similar to them developed by humans [64].

1.2.2 Lymphatic Vasculature and Reverse Cholesterol Transport

High plasma cholesterol levels, mainly high plasma LDL levels are one of the risk factors for developing atherosclerosis. Excess cholesterol is transported back to the liver for excretion via bile and stool in a process called reverse cholesterol transport (RCT). RCT is mainly facilitated by HDL, a member of the lipoprotein family, that is known to transport excess cholesterol back to the liver which takes up chylomicron remnants via the LDLR, the LDL receptor related protein and heparin sulfate proteoglycans which recognize apolipoproteins on the surface of remnant particles [65].

Lymphatic vessels have been found to participate in the removal of excess cholesterol via RCT in studies focusing on the lymphatic function of the skin.

Surgical disruption of lymphatic vessels in the popliteal area decreased RCT from the footpad of *ApoE*$^{-/-}$ mice by nearly 80%, whereas RCT was enhanced when lymphatic growth was induced by a lymphatic growth factor [66]. Martel *et al* showed that the disruption of tail lymphatics and injection of [^{3}H]-cholesterol-loaded macrophages into the tail distal to lymphatic disruption led to reduced [^{3}H]-cholesterol levels in plasma, liver and feces [67].

They also showed that lymphatics are important for the RCT from the arterial wall by transplanting the aorta of *ApoE*-deficient mice with [^{2}H]$_{6}$-labeled cholesterol into *ApoE* null recipients treated with a VEGFR3-blocking antibody, resulting in the fact that [^{2}H]$_{6}$-labeled cholesterol remained in the aorta of anti-VEGFR3 treated mice, but was removed

from the aorta of mice treated only with a control antibody [67]. These results suggest a possible role of lymphatic vessels in RCT.

1.2.3 Role of Lymphatic Vessels in the Development and Progress of Atherosclerosis

Lymphatic vessels have been found in the arterial wall more than a century ago and studies showed that they are mainly present in the arterial adventitia [68-70]. Their presence in the arterial wall as well as their involvement in lipoprotein metabolism and RCT animated research groups to investigate the possible involvement of the lymphatic vasculature in the development of atherosclerosis.

Studies showed that lymphatic capillaries in the adventitia of atherosclerotic plaques in humans and mice are dilated and their number and size increases with the progression of the disease [71].

Atherosclerotic lesions in young and intermediate cohorts of mice with lymphatic deficiency progressed faster than in control mice and had much less lymphatic vessels in the arterial wall [72].

Another study showed that early treatment with VEGF-C improved lymphatic transport in 6-week-old *Ldlr*$^{-/-}$ mice and subsequently limited plaque formation [73].

However, studies looking into whether stimulation of lymphatic function or lymphangiogenesis stimulates RCT from atherosclerotic arteries are extremely rare and further understanding of the lymphatic function in the lipoprotein metabolism and the development and progression of atherosclerosis, as well as sex-dependent differences, may lead to new avenues for the treatment of atherosclerosis and vascular diseases. The lymphatic vasculature and RCT might be used as possible targets to inhibit atherosclerotic lesion development.

1.3 Visualization of the Lymphatic System

1.3.1 Traditional Visualization Techniques of Lymphatic Vasculature

In the past decades, the lymphatic system has been getting less attention in research than the blood circulatory system. One of the reasons is that lymphatic vessels are more difficult to visualize and ex vivo preparation of lymphatic vessels needs special equipment and knowledge. The introduction of new visualization techniques and the development of various lymphatic specific markers such as LYVE1 and PROX1 have

helped to accelerate research and discoveries in the lymphatic field [9,23]. Knowledge has improved since then but the organ-specific role of lymphatic vessels, their important role in the maintenance of healthy organ function and the involvement of the lymphatic vasculature in the development and progression of diseases is still not clear yet, often because of lacking visualization methods.

Lymphatic vessels are widely visualized by immunostaining of sections, despite the fact that sections of organs only represent tiny parts of the organ. Sectioning of large organs is time consuming, and it is difficult to evaluate the lymphatic vasculature as a whole. Morphological changes of the lymphatic vasculature are difficult to capture and parameters such as total lymphatic area, total length of lymphatic vessels, but also lymphatic junctions and lymphatic end points cannot be assessed with the help of sections. Other visualization methods such as whole mount immunostaining or lymphatic reporter mouse models have other limitations, such as the strong background signal due to the opacity of tissues. The opacity of tissues allows assessment of only superficial lymphatic vessels and vessels in the depth of organs cannot be visualized. Therefore, it is necessary to have other ways to image these complex structures. One possibility is to use tissue clearing techniques.

1.3.2 Tissue-Clearing Techniques

Tissue opacity of native tissue is mainly caused by scattering and absorption of light and prevents sufficient imaging of the organ-specific lymphatic vasculature due to restricted light penetration [74]. To overcome this limitation, tissue-clearing was established, a technique that uses various approaches to make organs transparent and therefore reduce the opacity of tissue. A wide range of tissue-clearing techniques are available to date, but only a few are suitable for the acquisition of organ-specific lymphatic vasculature. Tissue-clearing protocols based on organic solvents such as Adipo-clear, CRISTAL, FASTClear, iDISCO and BABB often quench fluorescent signals and alter tissue morphology due to shrinkage [75-79]. Other protocols utilize expensive materials and solutions like the CLARITY protocol that utilizes FocusClear™ in combination with a complicated electrophoresis setup [80]. A tissue-clearing protocol that has been developed specifically to investigate the lymphatic system, WOBLI (whole organ blood and lymphatic vessel imaging), has extremely long incubation times of several months and is therefore not ideal

for everyday usage [81]. The most promising tissue-clearing protocol is CUBIC (clear, unobstructed brain/body imaging cocktails and computational analysis), that has reasonable clearing times and does not require any expensive solutions or complicated equipment [82-84]. CUBIC has constantly developed over the past years, but recent protocols require expensive light-sheet fluorescence microscopes and special computers to evaluate 3D images which can discourage many researchers from using tissue-clearing techniques on a regular basis [85-87].

The lack of efficient visualization methods for lymphatic vasculature underscores the need for advanced techniques to characterize lymphatics under both physiological and pathophysiological conditions, aiding in understanding their role in disease development.

2. Objectives

Lymphatic vessels are present in the arterial wall and participate in reverse cholesterol transport, suggesting a role in the development of atherosclerosis. However, their precise role in this disease remains largely unknown, primarily due to inefficient visualization techniques. During my PhD studies I aimed to:

- Develop an efficient approach to visualize the organ-specific lymphatic vasculature.
- Develop a straightforward, accessible method to quantify organ-specific lymphatic growth.
- Characterize the organ-specific lymphatic vasculature of the *Flt4*$^{kd/+}$ mouse model to visualize and quantify the organ-specific lymphatic vasculature.
- Visualize and characterize the lymphatic vasculature of the great vessels under physiological conditions in detail.
- Characterize atherosclerotic plaque development in the *Ldlr*$^{-/-}$ and *ApoE*$^{-/-}$ mouse model, two well-known atherosclerotic mouse models with focus on sex-dependent differences.
- Visualize and characterize the lymphatic vasculature of the *Ldlr*$^{-/-}$ mouse model in atherosclerosis.

3. Materials and Methods

3.1 Mouse Models

In this study, we used 3− to 5−month−old male and female *C57BL/6* and *Prox1*^{GFP} BAC transgenic lymphatic reporter mice to visualize lymphatic vasculature [88]. *Prox1*^{GFP} mice were maintained on a *C57BL/6* genetic background in heterozygous form and genotyped by a transgene specific PCR using 5′−GAT GTG CCA TAA ATC CCA GAG CCT AT−3′ forward and 5′−GGT CGG GGT AGC GGC TGA A−3′reverse primers. Additionally, we used 3− to 5−month−old *Flt4*$^{kd/+}$ mice, a previously described model for primary lymphedema, and their littermate control mice [89]. Mice carrying the kinase-dead *Flt4* allele (MRC Harwell, UK) were maintained on a NMRI background [89]. The *Flt4* point mutant allele was genotyped using 5′−CTGGCTGAGTCCCTAACTCG−3′ forward and 5'−CGGGGTCTTTGTAGATGTCC−3′reverse primers, followed by a restriction enzyme digestion with BglII, as previously described [39]. Furthermore, *Flt4*$^{+/+}$ and *Flt4*$^{kd/+}$ mice were crossed with the *Prox1*^{GFP} reporter strain, resulting in *Flt4*$^{+/+}$*; Prox1*^{GFP} and *Flt4*$^{kd/+}$*; Prox1*^{GFP} animals. *Flt4*$^{kd/+}$*; Prox1*^{GFP} were kept on a mixed background and tested for possible phenotype variations before used in our experiments. For the characterization of the lymphatic vasculature in atherosclerotic mice we used 20−weeks−old male and female *C57BL/6* control mice and 23−33−weeks−old *Ldlr*$^{-/-}$ and *ApoE*$^{-/-}$ mice, well−described mouse models of atherosclerosis [56-60,64,90]. Both atherosclerosis mouse models were maintained on a *C57BL/6* background. All animals were housed under a 12/12 h light/dark cycle with unrestricted access to food and water. All procedures were carried out according to the Animal Experimentation Review Board of Semmelweis University and the Government Office for Pest County, Hungary [I], [II].

3.2 Special Diet for Atherosclerosis Development

All mice of the atherosclerosis project received either a control diet (ssniff Spezialdiäten GmbH, E15720-04, Soest, Germany) with 5% crude fat and 0% cholesterol or a Western diet (ssniff Spezialdiäten GmbH, E15721-34, Germany) with 21% crude fat and 0.21% cholesterol for 20–30 weeks. Diets were initiated 21 days after birth, when the animals were separated from their mother. The mice had unrestricted access to food and water. The same number of mice with the same treatment period on control and Western diets was used to ensure comparability [II].

3.3 Body Weight and Serum Cholesterol Measurements

Body weight was measured at the end of the special diet, before the mice were euthanized at the beginning of an experiment. Serum was obtained through a cardiac puncture after 24 h of starvation, centrifuged at 12,500 rpm at 4 °C, and frozen at −80 °C until measured. Total cholesterol (Beckman Coulter, OSR6116, Brea, CA, USA), triglycerides (Beckman Coulter, OSR60118), HDL (Beckman Coulter, OSR6195), and LDL (Beckman Coulter, OSR6196) were measured with an AU chemistry analyzer (Beckman Coulter, AU480) according to the protocol of the manufacturer [II].

3.4 Paraffin-Based Histology and H/E staining

Mice were deeply anaesthetized by an intraperitoneal injection of 2.5% 2,2,2-Tribromoethanol (Sigma−Aldrich, T48402, St. Louis, MO, USA) and transcardially perfused with 10mL ice-cold phosphate-buffered saline (PBS)-Heparin (Teva Pharmaceuticals, Tel Aviv, Israel) (5000 IU/mL) followed by 10mL freshly prepared 4% paraformaldehyde (PFA) (Sigma−Aldrich, P6148, St. Louis, MO, USA). Tissue samples were collected and fixed overnight in 4% PFA at 4 °C, washed with PBS, dehydrated and embedded in paraffin using an embedding station (Leica, EG1150H, Wetzlar, Germany). A microtome (Thermo Fisher Scientific, HM340E, Waltham, MA, USA) was used to generate 7µm sections which were deparaffinized, rehydrated, and stained according to a widely available H/E staining protocol used in previous studies [39,40,91]. Images were acquired with an upright microscope (Nikon Instruments, ECLIPSE Ni-U, Tokyo, Japan) connected to a camera (Nikon Instruments, DS-Ri2) [I], [II].

3.5 Masson-Trichrome Staining of Paraffin Sections

The paraffin sections were deparaffinized, rehydrated, and stained with a Masson Trichrome Staining Kit (Sigma-Aldrich, HT15, St. Louis, MO, USA) according to the protocol of the manufacturer. Images were acquired with an upright microscope connected to a camera [II].

3.6 Alizarin Red S Staining of Paraffin Sections

To visualize plaque calcification in paraffin sections of the aorta, we deparaffinized sections, rehydrated and stained for 10mins at room temperature in 2% Alizarin Red in 1% KOH in distilled H_2O. The sections were then washed in 1% KOH in distilled H_2O, followed by a wash in PBS. Sections were dried, mounted and images were acquired with a stereo microscope connected to a camera [II].

3.7 Immunostaining of Sections

To perform immunostainings of sections, paraffin sections were deparaffinized, rehydrated, and stained with the lymphatic marker goat anti-LYVE1 (R&D Systems, AF2125, Minneapolis, MN, USA) in a dilution of 1:100 and anti-goat secondary antibody conjugated to Alexa Fluor 488 (Invitrogen, A11055, Waltham, MA, USA) in a dilution of 1:250. Nuclear staining with 4′ ,6-Diamidino-2- phenylindole (DAPI) helped to visualize the gross morphology of the section. Images were acquired with an upright microscope connected to a camera [I], [II].

3.8 Detection and Imaging of Native Fluorescence

Mice were deeply anaesthetized by an intraperitoneal injection of 2.5% 2,2,2-Tribromoethanol followed by cardiac perfusion with 10 mL ice-cold PBS-Heparin (5000 IU/mL). Tissue samples were collected, washed with PBS and visualized with a stereo microscope (Nikon Instruments, SMZ25, Tokyo, Japan) connected to a camera (Nikon Instruments, DS-Ri2, Tokyo, Japan) [I].

3.9 In Situ Brightfield Images of Aortas

To visualize the atherosclerotic plaque development in situ, mice were deeply anesthetized with an intraperitoneal injection of 2.5% 2,2,2- Tribromoethanol, followed by cardiac perfusion with 10 mL of ice cold PBS–Heparin (5000 IU/mL). Images were obtained in situ with a stereo microscope (Nikon Instruments, SMZ25, Tokyo, Japan) connected to a camera (Nikon Instruments, DS-Ri2, Tokyo, Japan) before the aortas were removed for further downstream experiments [II].

3.10 Whole-Mount Oil Red O Staining of Aortas

The mice were deeply anesthetized with an intraperitoneal injection of 2.5% 2,2,2-Tribromoethanol, followed by cardiac perfusion with 10 mL of ice cold PBS–Heparin (5000 IU/mL). The aortas were dissected and fixed overnight in 4% PFA at 4 °C. The aortas were washed with PBS, immersed in 60% Isopropanol, and incubated for 15 min in an Oil Red O solution (Sigma-Aldrich, O1391, St. Louis, MO, USA) at room temperature, 80 rpm, according to the protocol of the manufacturer. The stained aortas were washed in 60% Isopropanol for 3 min and then washed with PBS. Images were acquired with a stereo microscope connected to a camera [II].

3.11 Whole-Mount Alizarin Red S Staining of Aortas

The whole-mount Alizarin Red S staining was adapted from Kauffenstein *et al*. [92]. The mice were deeply anesthetized with an intraperitoneal injection of 2.5% 2,2,2-Tribromoethanol, followed by cardiac perfusion with 10 mL of ice cold PBS–Heparin (5000 IU/mL). The aortas were dissected and fixed overnight in 4% PFA at 4 °C. The aortas were washed with PBS and incubated in 0.003% Alizarin Red S (Sigma-Aldrich, A5533, St. Louis, MO, USA) and 1% KOH in distilled H_2O for 48 h at room temperature, 80 rpm. The stained aortas were washed for 3 min in 1% KOH in distilled H_2O and then washed with PBS. Images were acquired with a stereo microscope connected to a camera. The samples were stored long-term in 1:1 PBS/Glycerol (Sigma-Aldrich, G5516, St. Louis, MO, USA) [II].

3.12 Tissue Clearing and Whole-Mount Immunostaining

3.12.1 Cardiac Perfusion and Tissue Collection

Mice were deeply anaesthetized by an intraperitoneal injection of 2.5% 2,2,2-Tribromoethanol on day 0 and transcardially perfused with 10 mL ice-cold PBS-Heparin (5000 IU/mL) followed by 10 mL freshly prepared 2% PFA. Tissue samples were collected and fixed overnight in 2% PFA at 4 °C [I], [II].

3.12.2 Decolorization and Delipidation

Our tissue-clearing protocol is based on the previously published CUBIC protocol [82-84]. On day 1, the fixed samples were washed with PBS and immersed in Reagent 1 (25 wt% urea (Sigma-Aldrich, U5378, St. Louis, MO, USA), 25 wt% N, N, N′, N′−tetrakis (2-hydroxypropyl) ethylenediamine (Sigma-Aldrich, 122262, St. Louis, MO, USA) and 15 wt% Triton™ X-100 (Sigma-Aldrich, X100, St. Louis, MO, USA) in dest. H_2O). Incubation in Reagent 1 lasted for 5 days at 37 °C and 80 rpm. Reagent 1 was changed daily. On day 6, the transparent tissues were washed twice with PBS and rehydrated overnight in PBS, room temperature, 80 rpm [I], [II].

3.12.3 Whole-Mount Immunostaining

On day 7, the rehydrated tissue samples were stained for 4 days with the primary antibody(s) in Staining Solution 1 (serum (10%), sodium azide (0.2%), Tween® 20 (Sigma−Aldrich, P1379, St. Louis, MO, USA) (0.1%) in PBS with primary antibody(s) in the following dilutions: goat-anti-LYVE1 (Bio-Techne, AF2125, Minneapolis, MN, USA) in a dilution of 1:650, rabbit-anti-GFP (LifeTechnologies, A11122, Carlsbad, CA, USA) in a dilution of 1:500 and mouse-anti-αSMA (Sigma-Aldrich, A5228, St. Louis, MO, USA) in a dilution of 1:500) at 37 °C, 80 rpm. On day 11, the samples were washed with PBS-Tween® 20 (0.1%) for 2 h at room temperature, 80 rpm, and then stained for 3 days with the secondary antibody(s) in Staining Solution 2 (serum (2%), sodium azide (0.2%), PBS-Tween® 20 (0.1%) in PBS with secondary antibody(s) in the following dilutions: donkey-anti-goat Alexa Fluor 488 (Thermo Fisher Scientific, A11055, Waltham, MA, USA) in a dilution of 1:3000, donkey-anti goat Alexa Fluor 568 (Thermo Fisher Scientific, A11057, Waltham, MA, USA) in a dilution of 1:3000, donkey-anti-rabbit Alexa Fluor 488 (Thermo Fisher Scientific, A21206, Waltham, MA, USA) in a dilution of 1:3000 and donkey-anti-mouse Alexa Fluor 568 (Thermo Fisher Scientific, A10037, Waltham, MA, USA) in a dilution of 1:3000) at 37 °C, 80 rpm (tubes were wrapped in tinfoil to prevent degradation of the fluorophores during the incubation process). On day 14, stained tissues were washed for 2 h with PBS-Tween® 20 (0.1%) at room temperature, 80 rpm. Control stainings have been performed for all antibodies used in this study [I], [II].

3.12.4 Adjustment of the Refraction Indices (RI-Adjustment)

The stained samples were then incubated overnight in Reagent 2 (50 wt% sucrose (Sigma−Aldrich, S7903, St. Louis, MO, USA), 25 wt% urea, 10 wt% triethanolamine (Sigma−Aldrich, 90279, St. Louis, MO, USA), 0.1 wt% Triton™ X-100 in dest. H_2O) at 37 °C, 80 rpm. On day 15, samples were ready for imaging and were transferred to 4 °C for long-term storage [I], [II].

3.13 Microscopic Imaging and Processing

All images in this work were either acquired by upright microscopy or by stereo microscopy, both connected to a camera. Images were processed and analyzed using the NIS-Elements imaging software (Nikon Instruments, version BR 4.60.00) [I], [II].

3.14 Quantification of Cross-Sectional Atherosclerotic Plaque Area

To measure the atherosclerotic plaque size of the animals, we quantified the cross-sectional plaque size using H/E images or immune-stained paraffin sections (4× magnification). Cross-sectional plaque size was measured by Fiji (ImageJ, version 1.52p) [93]. Therefore, we measured the lumen of the vessel and the size of the plaque and calculated the percentage of vessel lumen restricted by the atherosclerotic plaque (normalized plaque size) [II].

3.15 Quantification of Fibrosis in Cross-Sections of the Aorta

To quantify atherosclerotic plaque fibrosis in cross-sections of the aorta, we used sections stained with Masson-Trichrome. Fibrotic areas were measured as well as the size of the atherosclerotic plaque and the percentage of the fibrotic area was quantified in relation to the plaque size (normalized plaque fibrosis) [II].

3.16 Manual Quantification of Lymphatic Structures in Paraffin Sections

The quantification of lymphatic structures in paraffin sections were performed manually using NIS-Elements. We quantified the lymphatic number, total lymphatic lumen, and average lymphatic lumen of one section (10× magnification) per mouse. To quantify the average lymphatic diameter of tissue-cleared aortas, we measured 30 lymphatic vessels (1.5× magnification) per mouse and calculated the average diameter [I], [II].

3.17 Quantification of Lymphatic Structures in Tissue-Cleared Samples with AngioTool

To quantify lymphatic structures in the tissue-cleared and whole-mount stained samples, we quantified total lymphatic area, total length of lymphatic vessels, lymphatic junctions and lymphatic end points with AngioTool, a free computational tool that has been developed for the quantitative analysis of vascular networks [94]. Images were uploaded into the program, followed by adjustment of parameters such as the vessel diameter and intensity and the removal of small particles from the calculation. All images were quantified using the same parameters to ensure comparability [I], [II].

3.18 Data Representation and Statistical Analysis

All figures shown in this work are representative images of the experiments. Representative images of the experiments are shown after the same treatment period. The same number of mice with the same treatment period on control and Western diets was used to ensure comparability. Data were statistically analyzed using the programs GraphPad Prism (version 7.03) and Excel (Microsoft, version 2018). All datasets were analyzed to identify outliers using the robust regression and outlier removal (ROUT) method, with a Q = 5%. The data points that were identified as outliers were removed from the dataset. All datasets were tested for normal distribution using the Shapiro–Wilk test, with an alpha = 0.01. The datasets showing normal distribution were compared with parametric tests including a one-way or two-way analysis of variance (ANOVA), followed by Tukey's post hoc test, while the datasets not following a normal distribution were compared with non-parametric tests, including the Kruskal–Wallis H-test, followed by Dunn's post hoc test. An alpha of <0.05 was considered to be significant [I], [II].

4. Results

The Results part is divided into two parts. In part one I am focusing on the organ-specific lymphatic vasculature and the development of a method to visualize and quantify lymphatic vasculature in healthy animals and animals with lymphatic deficiency.
Part two focuses on the visualization and quantification of atherosclerotic lesions and the characterization of lymphatic vessels in atherosclerotic mice.

4.1 Visualization of Organ-Specific Lymphatic Growth

4.1.1 Visualization of Lymphatics with Traditional Methods

To demonstrate the visualization of the lymphatic vasculature of different mouse organs with traditional methods, we used lymphatic reporter mice and immunostainings of paraffin sections. Initially, we visualized organ-specific lymphatic growth of the ear skin, small intestine, lungs and aorta of a *Prox1*^{GFP} lymphatic reporter mouse model, which expresses green fluorescent protein (GFP) in lymphatic endothelial cells (**Figure 3**).

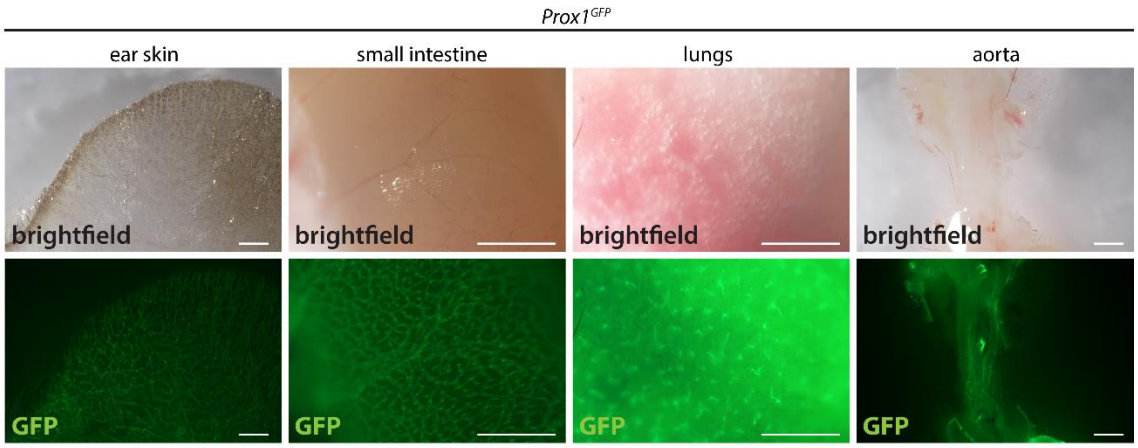

Figure 3: Visualization of the lymphatic vasculature in the *Prox1*^{GFP} lymphatic reporter mouse model. Detection of the native fluorescence of adult *Prox1*^{GFP} lymphatic reporter mice. Brightfield images of various organs and the GFP signals of those samples are shown. Images were acquired by stereo microscopy, scale bar 1000 µm (n = 10 organs of 10 mice). Representative images of the experiments are shown [I].

This traditional technique allowed only for the detection of superficial lymphatic vessels in these organs due to the opacity of native tissue. Next, we prepared paraffin sections of the ear skin, small intestine, lungs and aorta of *C57BL/6* mice, followed by an immunostaining of the sections against the lymphatic marker LYVE1.
The immunostainings enabled the detection of lymphatic vessels in the dermis of the ear

skin, in the submucosal layer of the intestine and lacteals in the villi of the intestine (**Figure 4**). We could detect lymphatic vessels surrounding the aorta and lymphatics near the bronchi of the lungs. Acquired images did not allow for a detailed assessment of lymphatic parameters such as the total length if lymphatic vessels, the total area of lymphatics or the number of lymphatic end points or junctions.

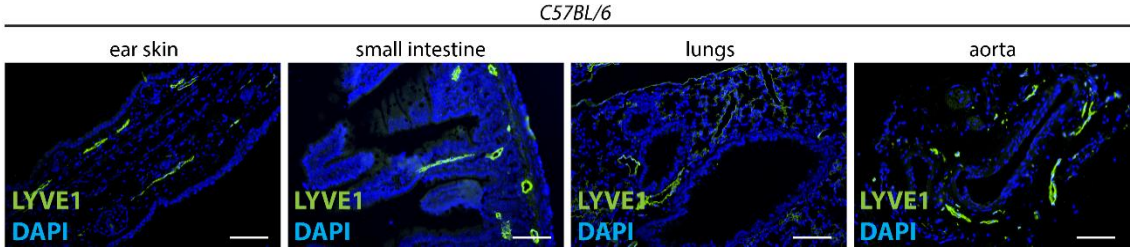

Figure 4: Visualization of lymphatics with immunostaining of paraffin sections. Visualization of lymphatic vessels in paraffin sections of adult *C57BL/6* mice stained with the lymphatic marker anti-LYVE1. Pictures were taken with upright microscopy, scale bar 100 µm (n = 10 organs of 10 mice). Representative images of the experiments are shown [I].

4.1.2 Our Optimized Tissue-Clearing Approach

To clear tissues, we optimized an existing tissue-clearing protocol with which we can clear various mouse organs without specialized equipment based on the CUBIC protocol by Susaki *et al.* [82,95]. The optimized protocol started on day 0 with a transcardial perfusion of the mouse, tissue collection and post-fixation in 2% PFA (**Figure 5**). The tissues were then decolorized with Reagent 1 for 5 days, a process that leads to transparent or "cleared" tissues. During this process, Reagent 1 was changed daily. After a rehydration and washing step with PBS, the tissues were stained with antibody containing Staining Solutions 1 and 2, followed by an overnight adjustment of the refraction indices (RI-matching) with Reagent 2. After the RI-matching, the tissues were ready for imaging.

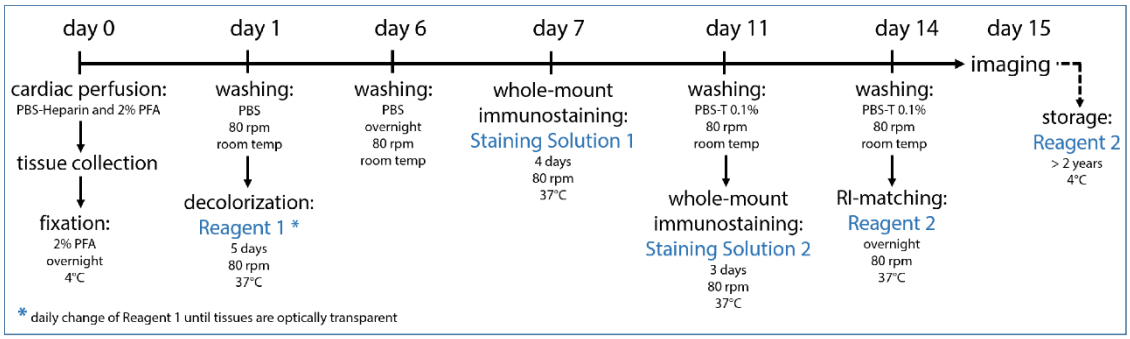

Figure 5: Optimized tissue-clearing protocol. Our optimized tissue-clearing protocol consists of an overnight fixation of the tissue sample, decolorization, whole-mount immunostaining with chosen antibodies and RI-matching before the sample is ready for imaging on day 15. Samples can be stored long-term at 4°C in Reagent 2 [I].

With this tissue-clearing protocol we could successfully clear the ear skin, small intestine, lungs, heart and aorta, uterus and ovaries, testicles and epididymis of the mouse (**Figure 6**). Tissue decolorization and RI-matching resulted in a high level of transparency.

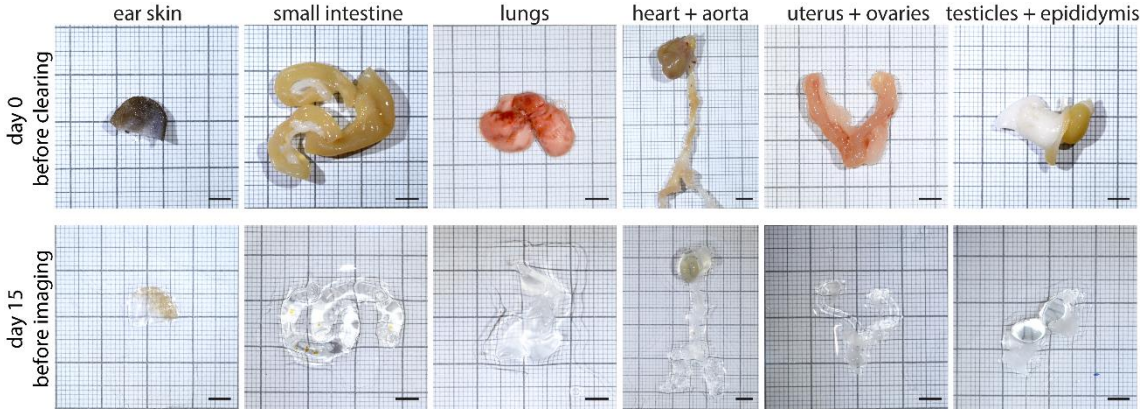

Figure 6: Tissue samples before and after the tissue-clearing protocol. Various organs of adult *C57BL/6* or *Prox1*^{GFP} mice are shown on day 0 before the start of our protocol and on day 15 before imaging. Scale bar 5 mm (n = 5 organs of 5 mice). Representative images of the experiments are shown [I].

4.1.3 Visualization of Lymphatic Vessels with Our Optimized Tissue-Clearing Protocol

To visualize the lymphatic vasculature of mouse organs with our optimized tissue-clearing protocol, we cleared organs of *C57BL/6* wild-type and *Prox1*^{GFP} lymphatic reporter animals, followed by a whole-mount immunostaining. We could demonstrate successful visualization of organ-specific lymphatic vessels. Utilizing this method, we effectively imaged the lymphatic network within the ear skin of *C57BL/6* mice via anti-LYVE1 staining. The images show the mouse ear at three distinct magnifications, revealing the presence of lymphatic capillaries within the skin (**Figure 7a**). Subsequently, we employed tissue-clearing techniques to examine the small intestines of *C57BL/6* mice, staining them with anti-LYVE1. Images captured at various magnifications demonstrate the feasibility of visualizing the intestinal lymphatic system using our method, even with only a stereo microscope, including the lymphatics in the submucosal area and the lacteals within the intestinal villi (**Figure 7b**). The lymphatic architecture of the lungs in *Prox1*^{GFP} mice was observed through anti-GFP staining, showcasing distinctive morphological features of lung lymphatics across different magnifications (**Figure 7c**).

Furthermore, we explored the lymphatic network surrounding the femoral arteries of *C57BL/6* mice using anti-LYVE1 staining. The provided images illustrate the presence of a lymphatic network surrounding the arteries (**Figure 7d**).

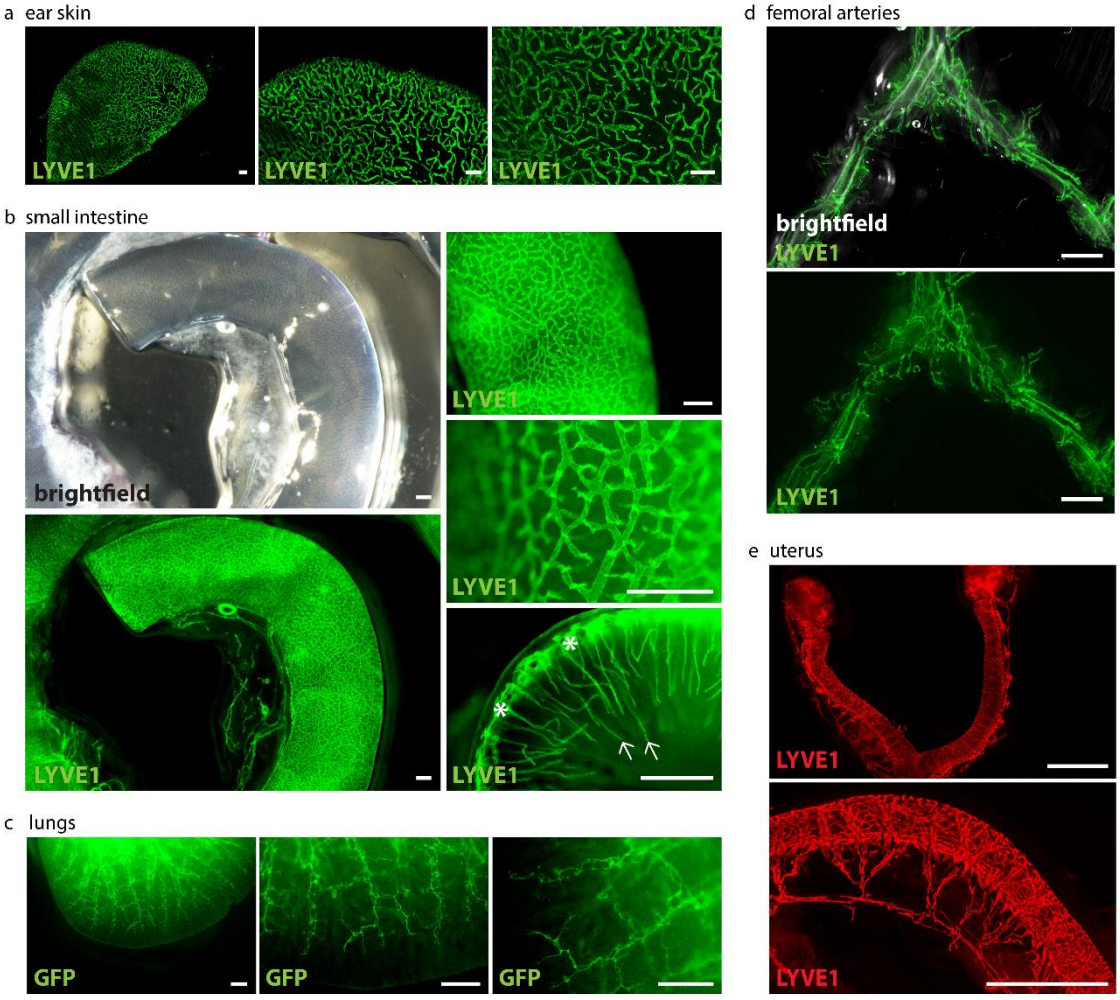

Figure 7: Visualization of organ-specific lymphatic vasculature by stereo microscopy. (a) Lymphatic vasculature of the ear skins of adult *C57BL/6* mice. Samples were stained with anti-LYVE1. Pictures were taken with a stereo microscope, scale bar 500 µm (n = 3 skin samples of 3 mice). **(b)** Lymphatic vasculature of the intestines of adult *C57BL/6* mice. Samples were stained with an anti-LYVE1 antibody. Villi intestinales are marked with arrows, the submucosal area is marked with asterisks. Pictures were taken with stereo microscopy, scale bar 500 µm (n = 3 small intestines of 3 mice). **(c)** Lymphatic vasculature of the lungs of adult *Prox1*^{GFP} mice. Samples were stained with an anti-GFP antibody. Pictures were taken with stereo microscopy, scale bar 500 µm (n = 3 lungs of 3 mice). **(d)** Lymphatic vasculature of the femoral arteries of adult *C57BL/6* mice. Samples were stained with an anti-LYVE1 antibody. Pictures were taken with stereo microscopy, scale bar 5000 µm (n = 6 femoral arteries of 6 mice). **(e)** Lymphatic vasculature of the uterus of adult *C57BL/6* mice. Samples were stained with an antiLYVE1 antibody. Pictures were taken with stereo microscopy, scale bar 2500 µm (n = 3 uteri of 3 mice) [I].

The lymphatic system within the uteri of C57BL/6 mice was examined using anti-LYVE1 staining. A structured network of lymphatic vessels surrounds both the uterine horns and the cervix (**Figure 7e**).

Next, we examined the cardiac lymphatics of *Prox1*^{GFP} mice utilizing an anti-GFP antibody for visualization, alongside an anti-vWF antibody (**Figure 8a**) or an anti-αSMA

antibody (**Figure 8b**) for blood vessel visualization, highlighting the vast potential of our methodology. This technique not only allows for the labeling of lymphatic markers but also facilitates the labeling of various other molecular markers using different antibodies in transparent tissues. Detailed visualization of lymphatic vessels surrounding coronary arteries was achieved through confocal microscopy.

Subsequently, we applied confocal microscopy to visualize the lymphatic network within the uteri of *Prox1*^{GFP} mice using anti-GFP and anti-vWF antibodies (**Figure 8c**). The image presents a magnified view of lymphatic and blood vessels within the uterine horn. Utilizing anti-GFP and anti-LYVE1 staining, we successfully visualized the lymphatic vasculature of the testicle and epididymis in *Prox1*^{GFP} mice (**Figure 8d**).

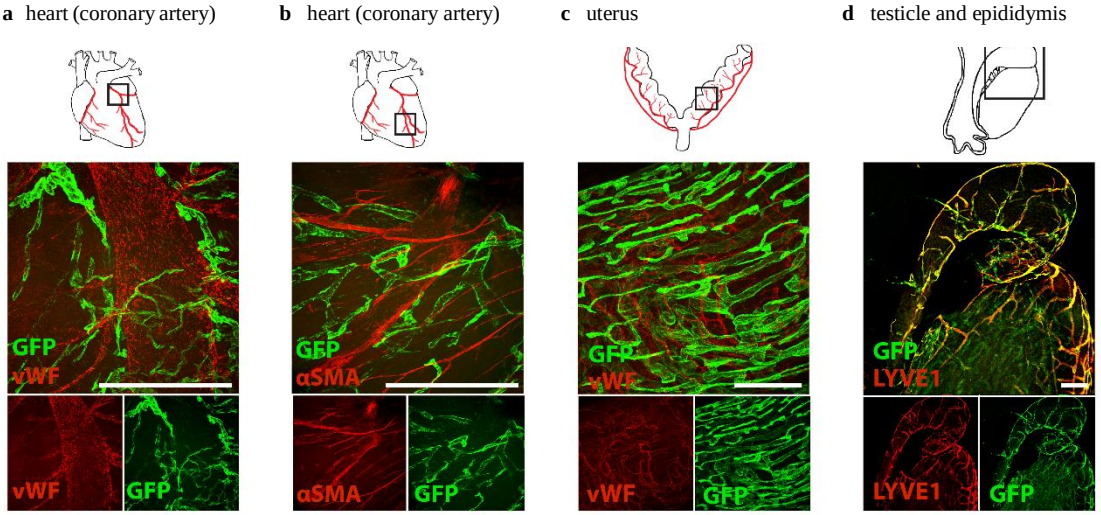

Figure 8: Visualization of organ-specific lymphatic vasculature by confocal microscopy. (**a**) Lymphatic vasculature of a coronary artery of a *Prox1*^{GFP} lymphatic reporter mouse. Sample was stained with an anti-GFP antibody and anti-von Willebrand Factor (vWF). Pictures were taken with confocal microscopy, scale bar 500 µm (n = 1 coronary artery). (**b**) Lymphatic vasculature of the coronary artery of an adult *Prox1*^{GFP} mouse. Sample was stained with an anti-GFP antibody and the smooth muscle marker anti-α-smooth muscle actin (αSMA). Pictures were taken with confocal microscopy, scale bar 500 µm (n = 1 coronary artery). (**c**) Lymphatic vasculature of the uteri of adult *Prox1*^{GFP} mice. Samples were stained with anti-GFP and anti-vWF antibodies. Pictures were taken with confocal microscopy, scale bar 500 µm (n = 2 uteri of 2 mice). (**d**) Lymphatic vasculature of the testicle and epididymis of an adult *Prox1*^{GFP} mouse. Sample was stained with anti-LYVE1 and with an anti-GFP antibody. Images were captured with confocal microscopy, scale bar 500 µm (n = 1 testicle with epididymis). Representative images of the experiments are shown [I].

Moreover, our investigation revealed that long-term storage of stained samples in Reagent 2 at 4°C did not diminish fluorescence signals. Even after 18 months, a robust and well-preserved fluorescent signal was still evident (**Figure 9**).

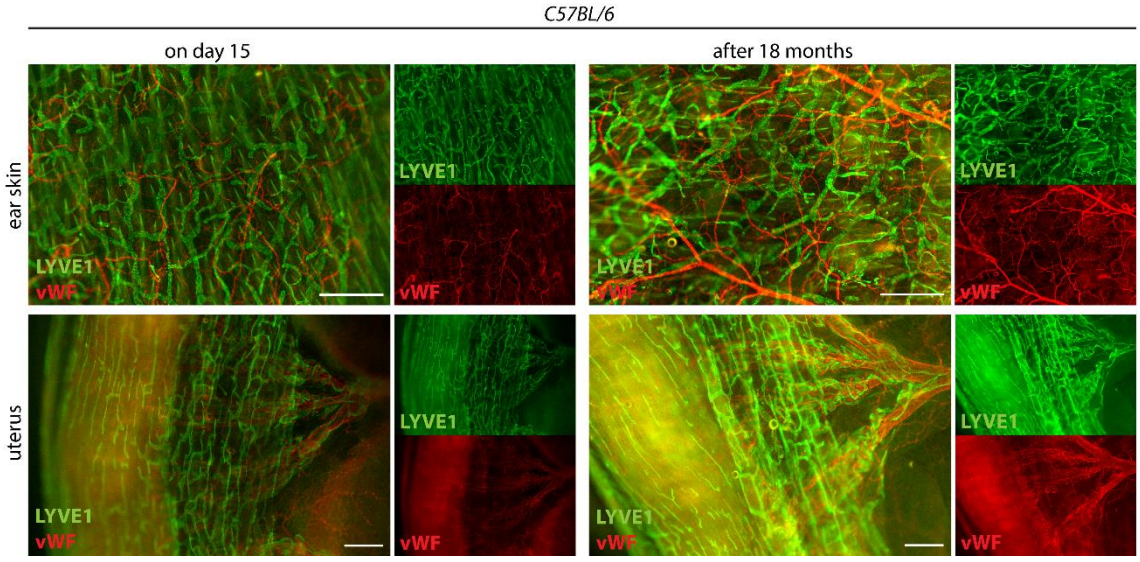

Figure 9: Long-term stability of the fluorescence signal. The tissue-cleared and stained ear skins and uteri of the *C57BL/6* mice are shown on day 15 at the end of the tissue-clearing protocol and 18 months later. Samples were stained with the lymphatic marker anti-LYVE1 and anti-von Willebrand Factor (vWF). Samples were stored at 4°C in Reagent 2. Images were acquired by stereo microscopy, scale bar 500 µm (n = 3 organs of 3 mice). Representative images of the experiments are shown [I].

4.1.4 Quantification of Lymphatic Structures with AngioTool

Analyzing 3D images can be time consuming and demanding, often necessitating specialized equipment like supercomputers and dedicated software. To streamline this process for assessing lymphatic vasculature images, we evaluated AngioTool, a freely available computational tool initially designed for vascular network analysis [94]. Employing AngioTool, we quantified lymphatic junctions and endpoints across four distinct confocal images of the small intestines of *Prox1*^{GFP} mice (**Figure 10**).

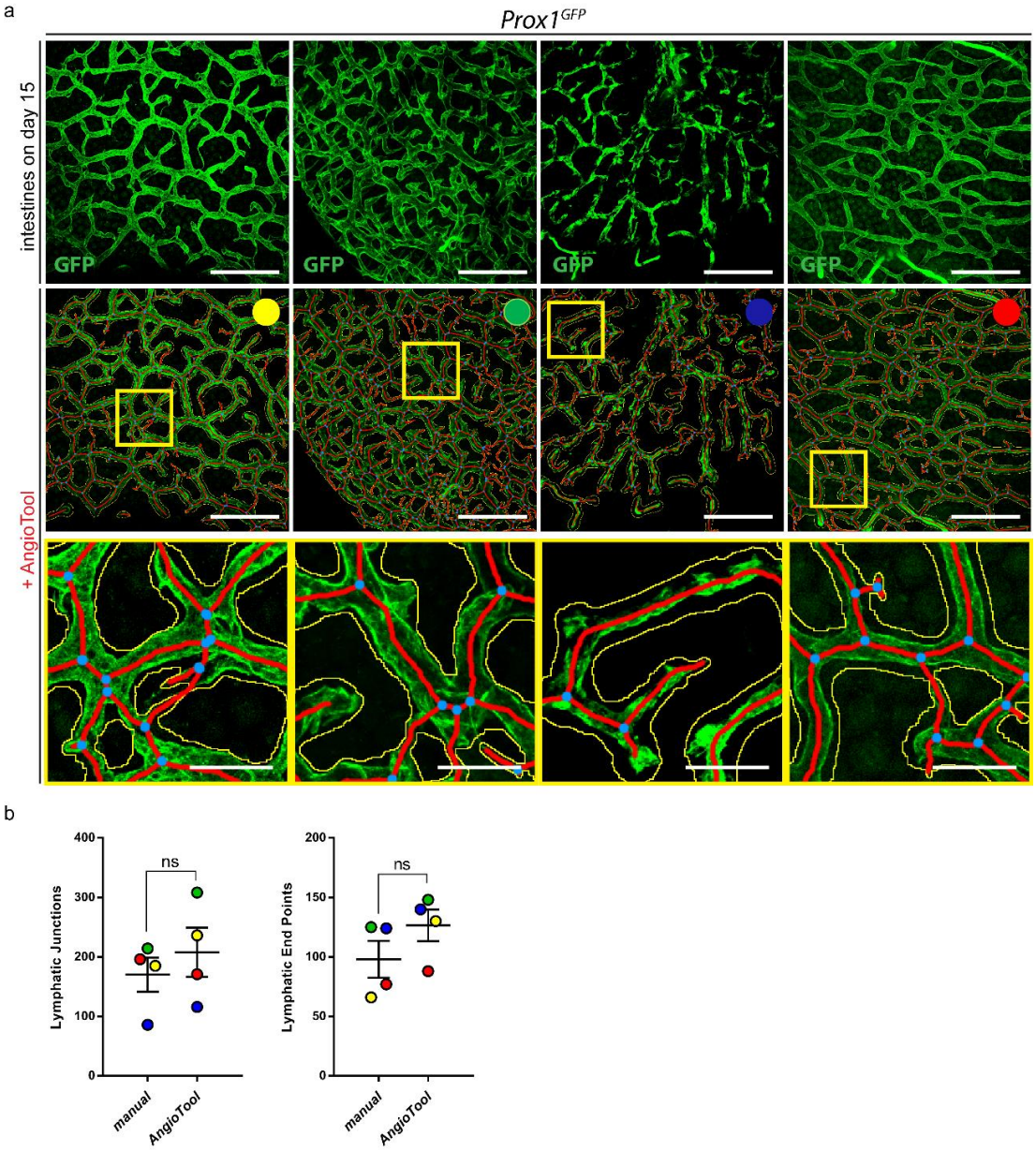

Figure 10: Quantification of organ-specific lymphatic vasculature. (**a)** Lymphatic vasculature of the small intestines of four *Prox1*^{GFP} mice on day 15 after the tissue-clearing protocol. Samples were stained with an anti-GFP antibody. Images were acquired by confocal microscopy, scale bar 500 µm. Images were quantified with AngioTool, a user-friendly tool for the quantification of vasculature. Every sample is marked with a specific color to analyze the results of the individual samples. Magnification of the images shows the quantification of AngioTool in detail: blue dots represent lymphatic junctions and red lines mark the length and the end points of lymphatic vessels. The yellow line surrounds the lymphatic area. Scale bar 20 µm. (**b)** Comparison of manual and AngioTool quantifications of the lymphatic junctions and lymphatic end points of the intestines shown in (a). Lymphatic junctions and lymphatic end points were quantified either manually with NIS-Elements imaging software or with AngioTool. Data are represented as mean ± SEM. Samples were statistically analyzed by a two-tailed, paired t-test; $p = 0.2266$ for lymphatic junctions, $p = 0.0996$ for lymphatic end points; ns = not significant; n = 4 small intestines of 4 mice [I].

In order to assess if AngioTool's quantifications meets our needs, we manually quantified the lymphatic junctions and endpoints within the same images for comparison. Each image was color-marked for individual analysis. Upon comparison, we found no significant difference between the manually quantified images and those processed with AngioTool (**Figure 10b**).

4.1.5 Morphological Changes of the Organ-Specific Lymphatic Vasculature of *Flt4$^{kd/+}$* Mice

To test the developed approach, we visualized the organ-specific lymphatic growth in *Flt4$^{kd/+}$* mice with our optimized tissue-clearing technique on various organs of both *Flt4$^{+/+}$* and *Flt4$^{kd/+}$* mice bred with the *Prox1^{GFP}* transgenic reporter strain. Initially, we examined the skin of *Flt4$^{+/+}$; Prox1^{GFP}* and *Flt4$^{kd/+}$; Prox1^{GFP}* mice, employing an anti-GFP antibody along with anti-von Willebrand Factor (vWF) staining. *Flt4$^{+/+}$; Prox1^{GFP}* mice exhibited a typical network of blood and lymphatic vessels within the skin (**Figure 11a**). Conversely, *Flt4$^{kd/+}$; Prox1^{GFP}* mice displayed normal blood vessels but lacked detectable lymphatic vessels in the skin.

Subsequently, we visualized the lymphatic vasculature of the intestines in *Flt4$^{+/+}$; Prox1^{GFP}* and *Flt4$^{kd/+}$; Prox1^{GFP}* mice using an anti-GFP antibody coupled with anti-LYVE1 staining. *Flt4$^{+/+}$; Prox1^{GFP}* mice showcased the typical morphology of the intestinal lymphatic vasculature, with clearly discernible GFP-positive nuclei of lymphatic endothelial cells within the lymphatic structures (**Figure 11b**). In contrast, *Flt4$^{kd/+}$; Prox1^{GFP}* mice exhibited significantly enlarged and dilated lymphatic vessels in the intestines compared to their control littermates.

Lastly, we examined the lymphatic vasculature of the lungs in *Flt4$^{+/+}$; Prox1^{GFP}* and *Flt4$^{kd/+}$; Prox1^{GFP}* mice utilizing an anti-GFP antibody.

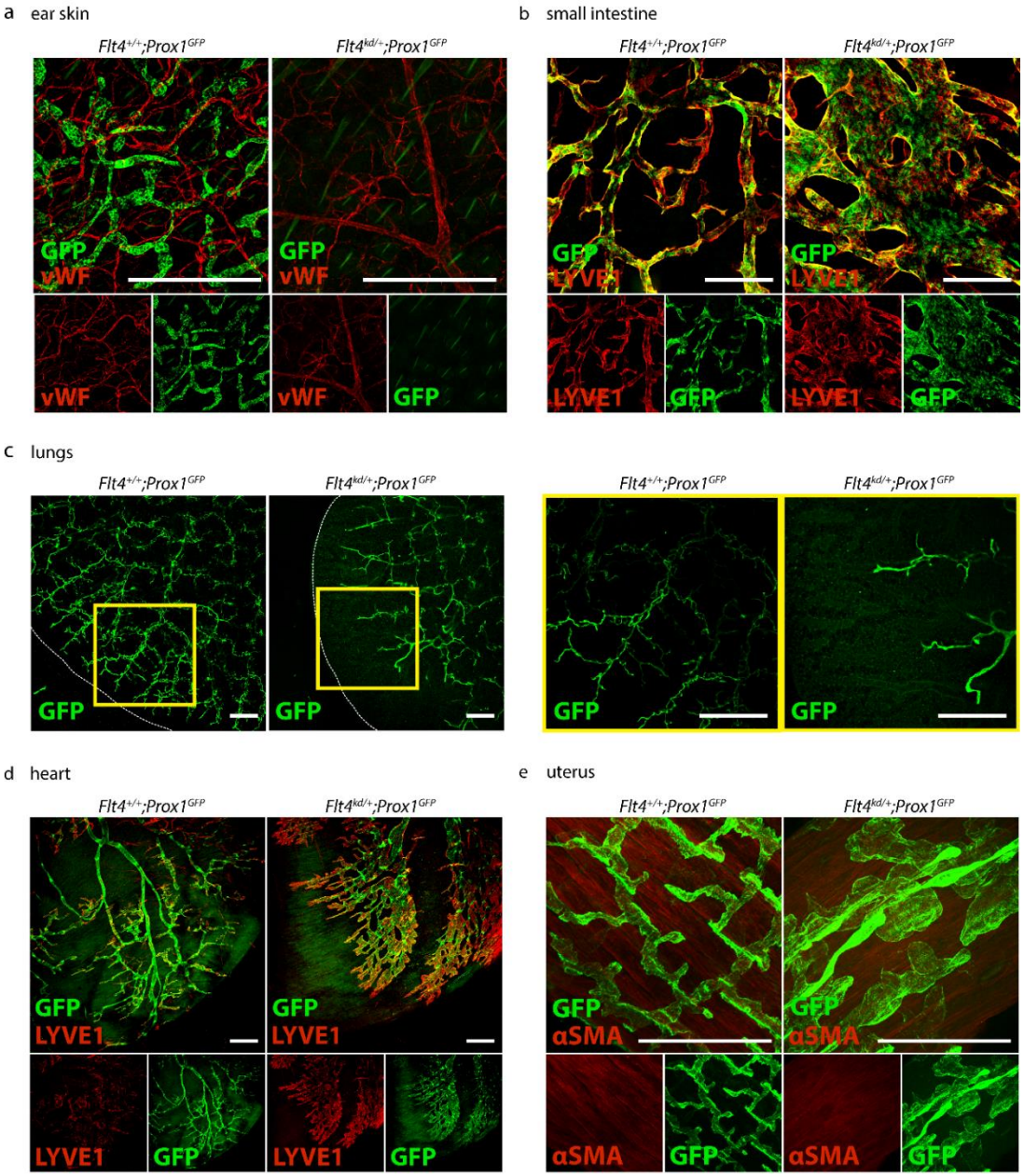

Figure 11: Visualization of the organ-specific lymphatic vasculature of *Flt4$^{kd/+}$* mice. (a) Lymphatic vasculature of the ear skins of adult *Flt4$^{+/+}$; Prox1^{GFP}* and *Flt4$^{kd/+}$; Prox1^{GFP}* mice. Ears were stained with an anti-GFP antibody and anti-von Willebrand Factor (vWF). Images were acquired by confocal microscopy, scale bar 500 µm (n = 5 ears of 5 mice per group). **(b)** Lymphatic vasculature of the small intestines of adult *Flt4$^{+/+}$; Prox1^{GFP}* and *Flt4$^{kd/+}$; Prox1^{GFP}* mice. Intestines were stained with an anti-GFP antibody and anti-LYVE1. Pictures were taken with confocal microscopy, scale bar 500 µm (n = 6 small intestines of 6 mice per group). **(c)** Lymphatic vasculature of the lungs of adult *Flt4$^{+/+}$; Prox1^{GFP}* and *Flt4$^{kd/+}$; Prox1^{GFP}* mice. Lungs were stained with an anti-GFP antibody. Images were taken with a confocal microscope, scale bar 500 µm (n = 3–4 lungs of 3–4 mice per group). **(d)** Lymphatic vasculature of the hearts of adult *Flt4$^{+/+}$; Prox1^{GFP}* and *Flt4$^{kd/+}$; Prox1^{GFP}* mice. Hearts were stained with an anti-GFP antibody and anti-LYVE1. Images were taken with confocal microscopy, scale bar 500 µm (n = 3–4 hearts of 3–4 mice per group). **(e)** Lymphatic vasculature of the uteri of adult *Flt4$^{+/+}$; Prox1^{GFP}* and *Flt4$^{kd/+}$; Prox1^{GFP}* mice. Uteri were stained with an anti-GFP antibody and anti-alpha smooth muscle actin (αSMA). Images were acquired by confocal microscopy, scale bar 250 µm (n = 3–4 uteri of 3–4 mice per group). Representative images of the experiments are shown [I].

Flt4$^{kd/+}$*; Prox1*^{GFP} mice exhibit a reduced number of lymphatic structures in the lungs compared to their littermate controls, with those present being notably dilated (**Figure 11c**). Furthermore, the lymphatic vasculature did not extend to the periphery of the lungs. Moving on, we investigated the organ-specific lymphatic vasculature of the heart in *Flt4*$^{+/+}$*; Prox1*^{GFP} and *Flt4*$^{kd/+}$*; Prox1*^{GFP} mice, utilizing an anti-GFP antibody alongside the lymphatic marker anti-LYVE1. *Flt4*$^{kd/+}$*; Prox1*^{GFP} mice displayed markedly dilated lymphatic vessels in the heart (**Figure 11d**).

Lastly, we examined the lymphatic vasculature of the uteri in *Flt4*$^{+/+}$*; Prox1*^{GFP} and *Flt4*$^{kd/+}$*; Prox1*^{GFP} mice, employing an anti-GFP antibody and the smooth muscle marker anti-alpha smooth muscle actin (αSMA). It was observed that *Flt4*$^{kd/+}$*; Prox1*^{GFP} mice exhibited highly dilated and morphologically altered lymphatic vessels in the uterus (**Figure 11e**).

4.1.6 Quantification of Morphological Changes of the Lymphatic Vasculature of *Flt4*$^{kd/+}$ mice

To show the benefits of our methodology, we conducted image quantification on sections of the lung and small intestine, as well as on images of tissue-cleared lungs and intestines. Paraffin-based histology was carried out on lung and small intestine samples from both *Flt4*$^{+/+}$*; Prox1*^{GFP} and *Flt4*$^{kd/+}$*; Prox1*^{GFP} mice. These samples were stained using an anti-GFP antibody and anti-LYVE1. We manually quantified the lung section images using NIS-Elements imaging software. The quantifications revealed no significant differences in the number of lymphatics, total lymphatic lumen, or average lymphatic lumen in the lungs between *Flt4*$^{kd/+}$*; Prox1*^{GFP} mice and their littermate controls (**Figure 12a**).

Subsequently, we manually quantified the small intestine section images with NIS-Elements. The results showed a significant decrease in the number of intestinal lymphatics in *Flt4*$^{kd/+}$*; Prox1*^{GFP} mice. Additionally, both the total lymphatic lumen and the average lymphatic lumen were significantly increased in the small intestines of *Flt4*$^{kd/+}$*; Prox1*^{GFP} mice compared to their littermate controls (**Figure 12a**).

To highlight the advantages of our approach, we tissue-cleared and stained lungs and small intestines of *Flt4*$^{+/+}$*; Prox1*^{GFP} and *Flt4*$^{kd/+}$*; Prox1*^{GFP} mice and acquired confocal images of the samples. Quantifications of the tissue-cleared lungs revealed a decreased total lymphatic area, reduced total length of lymphatic vessels, fewer lymphatic junctions,

and fewer lymphatic endpoints in *Flt4$^{kd/+}$; Prox1^{GFP}* mice compared to their controls. However, there was a significant increase in lymphatic diameter (**Figure 12a**).

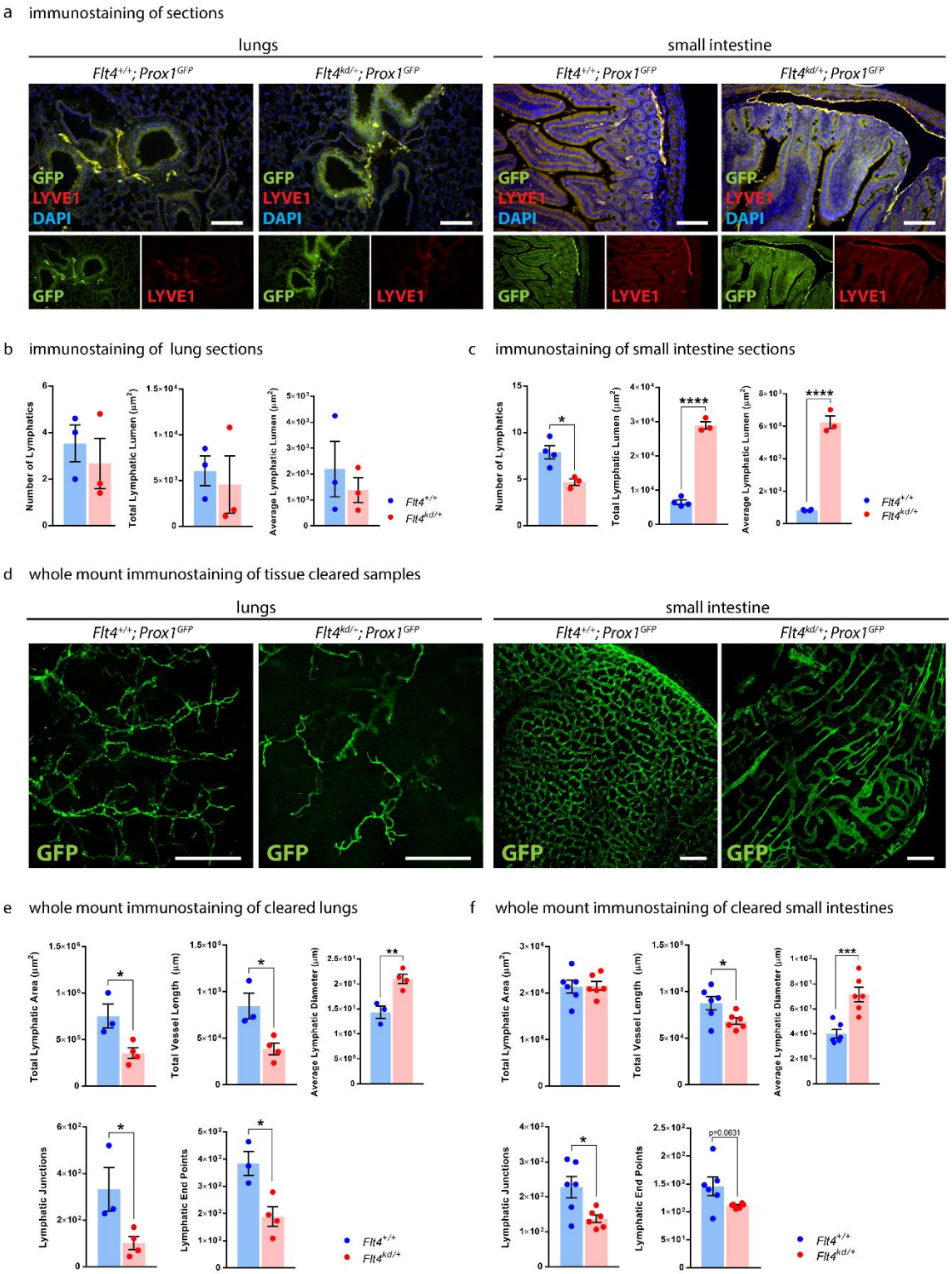

Figure 12: Visualization and quantification of the organ-specific lymphatic vasculature of Flt4$^{kd/+}$ mice. (a) Visualization of the organ-specific lymphatic vasculature of the lungs and intestines of adult *Flt4$^{+/+}$; Prox1^{GFP}* and *Flt4$^{kd/+}$; Prox1^{GFP}* mice by immunostaining of sections. Sections were stained with an anti-GFP antibody and anti-LYVE1. Pictures were acquired by upright microscopy, scale bar 100 µm. Quantifications of the lung sections (**b**) and the small intestine sections (**c**) were performed manually using NIS-Elements imaging software and include the number of lymphatics, the total lymphatic lumen and the average lymphatic lumen per field of view. Data are represented as mean ± SEM. Samples were statistically analyzed by a two-tailed, unpaired t-test; $p = 0.5502$ for the number of lymphatics in the lung sections, $p = 0.6925$ for the total lymphatic lumen of the lung sections, $p = 0.5262$ for the average lymphatic lumen of the lung sections, $p = 0.0152$ for the number of lymphatics in the small intestine sections, $p < 0.0001$ for the total lymphatic lumen of the small intestine sections and $p < 0.0001$ for the average lymphatic lumen of the small intestine sections; * $p < 0.05$; **** $p < 0.0001$; n = 3–4 lungs or small intestines of 3–4 mice per group. (**d**) Tissue-cleared lungs and intestines of adult *Flt4$^{+/+}$; Prox1^{GFP}* and *Flt4$^{kd/+}$; Prox1^{GFP}* mice. Samples were stained with an anti-GFP antibody. Images were acquired by confocal microscopy, scale bar 500 µm. Quantifications of the tissue-cleared lungs (**e**) and small intestines (**f**) were quantified with AngioTool and include the total lymphatic area, the total vessel length, lymphatic junctions and lymphatic end points per field of view. Lymphatic diameters were quantified manually using NIS-Elements. Data are represented as mean ± SEM. Samples were statistically analyzed by a two-tailed, unpaired t-test; $p = 0.0256$ for the total lymphatic area of tissue-cleared lungs, $p = 0.0202$ for the total vessel length of tissue-cleared lungs, $p = 0.0068$ for the average lymphatic diameter of tissue-cleared lungs, $p = 0.0427$ for the lymphatic junctions of tissue-cleared lungs, $p = 0.0173$ for the lymphatic end points of tissue-cleared lungs, $p = 0.9156$ for the total lymphatic area of tissue-cleared small intestines, $p = 0.0377$ for the total vessel length of tissue-cleared intestines, $p = 0.0008$ for the average lymphatic diameter of tissue-cleared small intestines, $p = 0.0181$ for the lymphatic junctions of tissue-cleared small intestines and $p = 0.0631$ for the lymphatic end points of tissue-cleared small intestines; * $p < 0.05$; ** $p < 0.01$; *** $p < 0.001$; n = 3–6 lungs or small intestines of 3–6 mice per group. Representative images of the experiments are shown [I].

Our findings indicate that *Flt4$^{kd/+}$; Prox1^{GFP}* mice have significantly fewer but dilated lymphatic vessels in the lungs. Quantifications of the tissue-cleared small intestines showed no difference in the total lymphatic area; however, there was a significant decrease in the total length of lymphatic vessels, fewer lymphatic junctions, and fewer lymphatic endpoints in *Flt4$^{kd/+}$; Prox1^{GFP}* mice compared to their controls, along with a significant increase in lymphatic diameter. These results suggest that *Flt4$^{kd/+}$; Prox1^{GFP}* mice have fewer but dilated lymphatic vessels in the small intestine. Overall, our approach effectively detects morphological changes in the lymphatic vasculature, particularly changes in parameters such as total lymphatic area, total length of lymphatic vessels, lymphatic junctions, and endpoints [II].

4.2 Characterization of the Lymphatic Vasculature in Atherosclerosis

4.2.1 Characterization of the Lymphatic Vasculature in Different Segments of the Great Vessels

To investigate the lymphatic vascularization of the arterial wall, we sectioned and stained different segments of the aorta from *C57BL/6* wild-type mice using the lymphatic marker anti-LYVE1. We did not detect lymphatic vessels in the arterial wall of the aortic arch; however, lymphatic vessels were present in the arterial walls of other segments of the aorta, including the thoracic aorta, abdominal aorta, and femoral arteries (**Figure 13**).

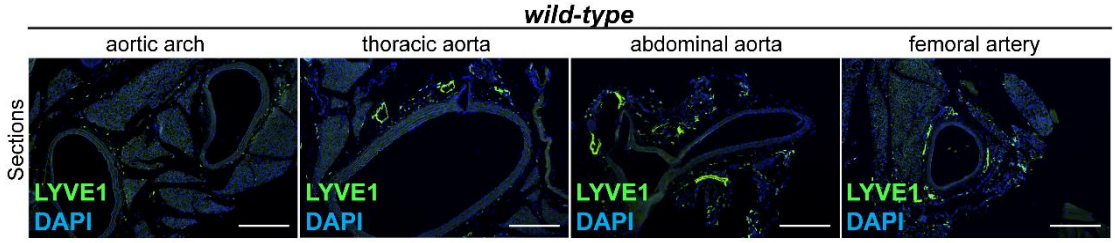

Figure 13: Lymphatic vasculature of the arterial wall. Lymphatic vessels in the arterial wall of the aorta of male *C57BL/6* mice. Sections of the aortic arch, thoracic aorta, abdominal aorta and femoral arteries were stained with the lymphatic marker anti-LYVE1. Images were acquired by upright microscopy; scale bars = 250 µm, n = 6 aortas of 6 mice. Representative images of the experiments are shown [II].

To further investigate the lymphatic vasculature of the aorta, we tissue-cleared and stained aortas from *C57BL/6* wild type mice using anti-LYVE1. We then quantified the total lymphatic area, the length of lymphatic vessels, the number of lymphatic endpoints, and lymphatic junctions using AngioTool, a method we have previously described [95]. Our findings showed no detectable lymphatic vessels in the arterial wall of the aortic arch.

However, lymphatic vessels were present in the thoracic aorta, abdominal aorta, and femoral arteries (**Figure 14a**). Quantitative analysis of the images revealed significant differences in the total lymphatic area, the total length of lymphatic vessels, the number of lymphatic junctions, and the number of lymphatic endpoints across different segments of the aorta (**Figure 14b**). These results suggest that lymphatic vascularization of the arterial wall varies significantly between different aortic segments, with few to no lymphatic vessels in the aortic arch, more in the thoracic aorta, and the highest density in the abdominal aorta and femoral arteries.

a

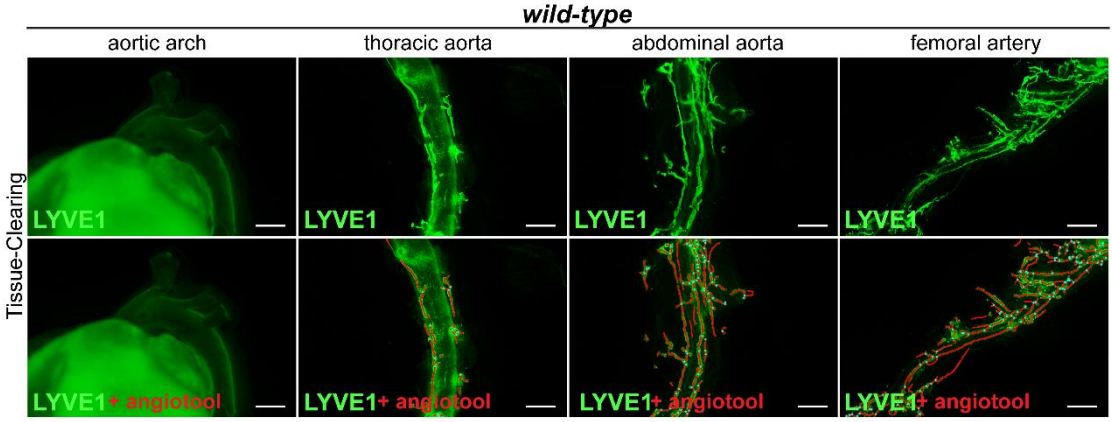

b

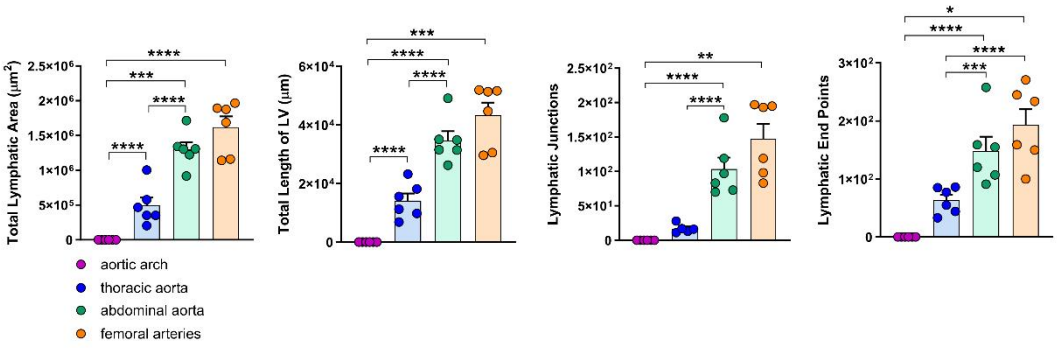

Figure 14: Visualization and quantification of the lymphatic vasculature in the arterial wall. (a) Lymphatic vessels in the tissue-cleared aorta of male *C57BL/6* mice stained with anti-LYVE1. Lower images show the quantification of the lymphatic vasculature with AngioTool. Images were acquired by stereo microscopy; scale bars = 1000 µm, n = 6 aortas of 6 mice. **(b)** Quantification of the lymphatic vasculature of tissue-cleared aortas of male *C57BL/6* mice. The total lymphatic area, total length of LV, lymphatic junctions and lymphatic end points were quantified using AngioTool. Data are represented as mean ± SEM and were statistically analyzed by a one-way ANOVA test, p -values < 0.05 were considered to be significant and indicated by asterisks; * $p < 0.05$; ** $p < 0.01$; *** $p < 0.001$; **** $p < 0.0001$; n = 6 aortas of 6 mice per group. Representative images of the experiments are shown [II].

4.2.2 Western Diet Leads to Elevated Body Weight and Serum Lipids in Male and Female Mice

To characterize the atherosclerotic mouse models used in our study, we measured the body weight of male and female *Ldl*$^{-/-}$ and *ApoE*$^{-/-}$ mice on a control or Western diet.

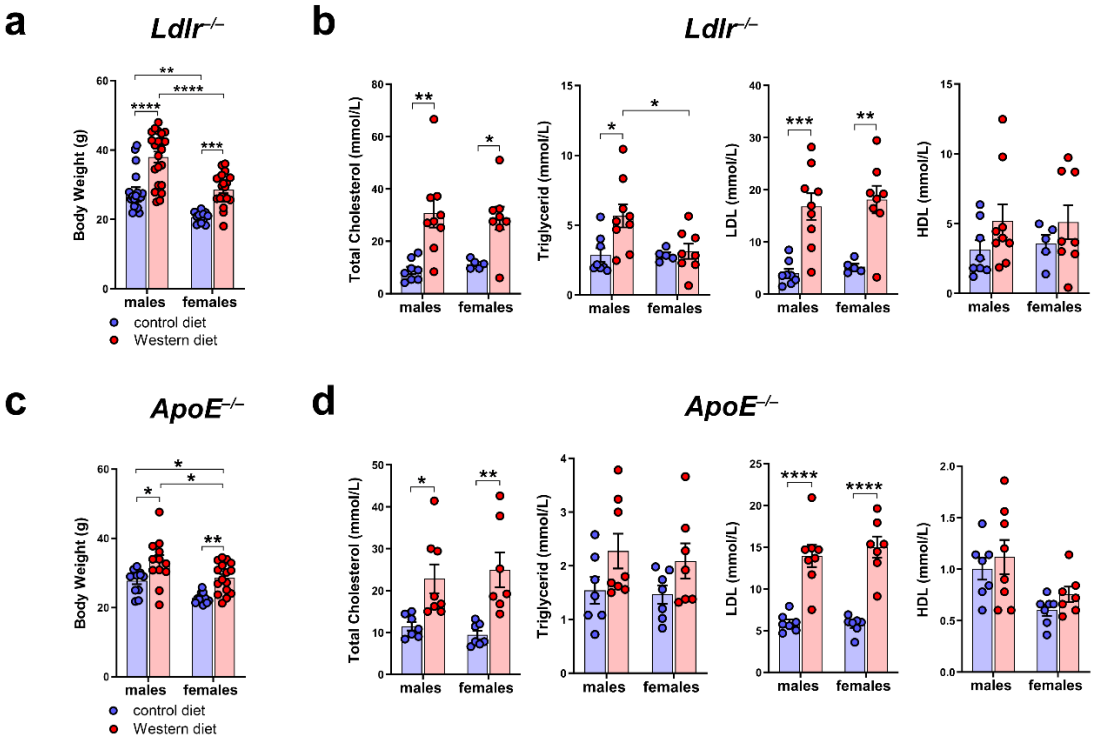

Figure 15: Body weight and serum cholesterol levels of *Ldlr*$^{-/-}$ and *ApoE*$^{-/-}$ mice. (a) Body weight of male and female *Ldlr*$^{-/-}$ mice after 20–30 weeks on control or Western diet; n > 10 mice per group. **(b)** Serum cholesterol levels of male and female *Ldlr*$^{-/-}$ after 20–30 weeks on control or Western diet; n = 5–9 serum samples of 5–9 mice per group. **(c)** Body weight of male and female *ApoE*$^{-/-}$ mice after 22–30 weeks on control or Western diet; n > 10 mice per group. **(d)** Serum cholesterol levels of male and female *ApoE*$^{-/-}$ after 22–30 weeks on control or Western diet. Data are represented as mean ± SEM and were statistically analyzed by a two-way ANOVA test; *p*-values < 0.05 were considered to be significant and indicated by asterisks; * $p < 0.05$; ** $p < 0.01$; *** $p < 0.001$; **** $p < 0.0001$; n = 7–8 serum samples of 7–8 mice per group [II].

The results indicated a significant increase in body weight for both *Ldlr*$^{-/-}$ and *ApoE*$^{-/-}$ mice when fed a Western diet (**Figure 15a** and **c**). Notably, male mice exhibited a significantly higher body weight compared to females, regardless of being on a control or Western diet. To analyze blood lipid profiles, we measured total cholesterol, triglycerides, HDL, and LDL levels in the serum of male and female *Ldlr*$^{-/-}$ and *ApoE*$^{-/-}$ mice on both diets. The analysis showed that total cholesterol levels were markedly elevated in both *Ldlr*$^{-/-}$ and *ApoE*$^{-/-}$ mice on the Western diet, which was mainly due to

a significant rise in serum LDL levels (**Figure 15b** and **d**). Despite the substantially higher body weight in males fed the Western diet, no sex-related differences were found in the serum lipid levels between males and females.

4.2.3 Female Mice Tend to Develop Larger Plaques Than Males When Fed a Western Diet

To assess the development of atherosclerotic plaques, we initially examined the in situ plaque formation in the aortic arch of *Ldlr*$^{-/-}$ mice subjected to either a control diet or a Western diet over various time intervals. The onset of lipid accumulation in the aortic arch of *Ldlr*$^{-/-}$ mice was observable after 16 weeks on the Western diet, progressing to a severe state by the 20th week on the Western diet (**Figure 16**).

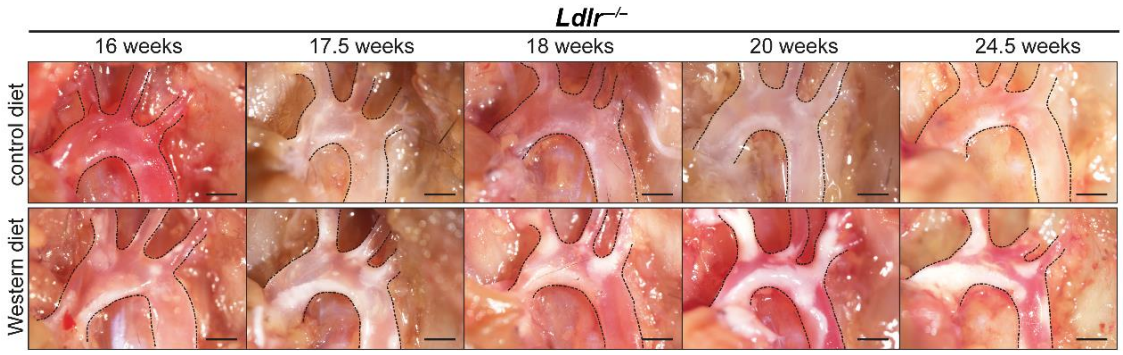

Figure 16*: In situ* atherosclerotic plaque development in *Ldlr*$^{-/-}$ mice. *In situ* plaque development in the aortic arch of female *Ldlr*$^{-/-}$ mice on control or Western diet at various time points. Images were acquired by stereo microscopy, scale bar = 1000 µm, n = 10 aortas of 10 mice. Representative images of the experiments are shown [II].

Paraffin-based histology and H/E staining of the aorta from *Ldlr*$^{-/-}$ mice under both control and Western dietary conditions were used to evaluate the cross-sectional plaque area in various segments of the aorta (**Figure 17a**). Manual assessments revealed a significantly greater cross-sectional plaque area in *Ldlr*$^{-/-}$ mice on the Western diet compared to those on the control diet, with the largest plaque areas observed in the brachiocephalic artery and the aortic arch (**Figure 17b**). Notably, no plaques were detected in the femoral arteries. Additionally, female mice on the Western diet displayed a tendency towards larger cross-sectional plaque areas in the aortic arch compared to males (**Figure 17b**).

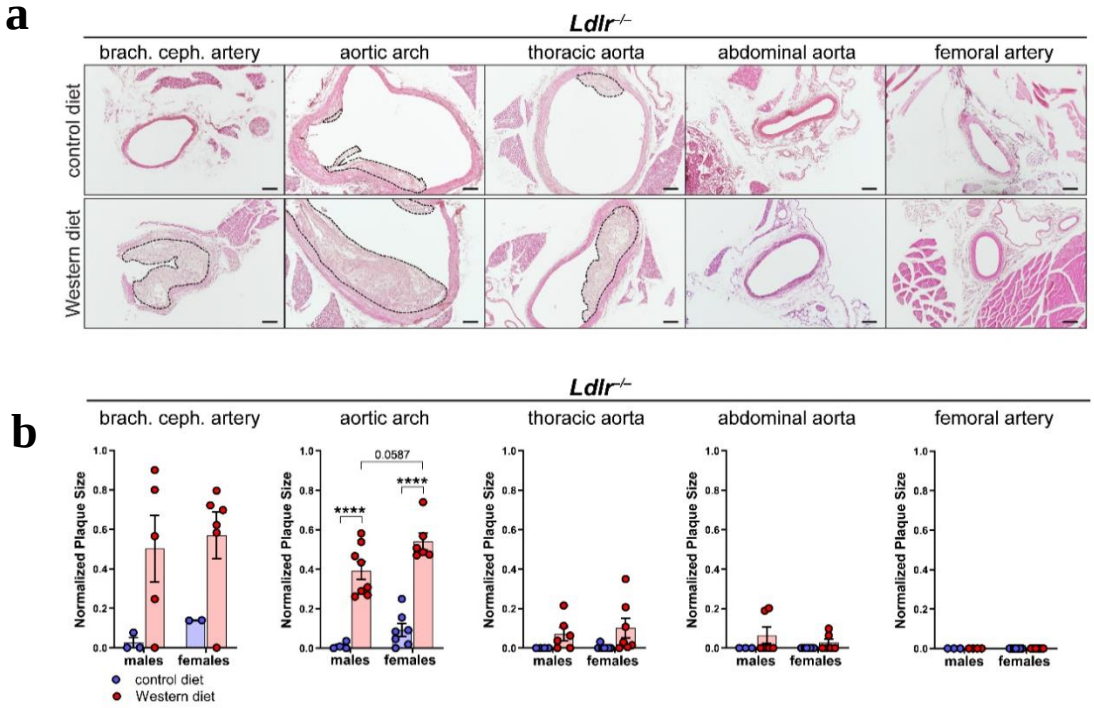

Figure 17*:* Visualization and Quantification of plaques throughout the arterial tree of *Ldlr*$^{-/-}$ mice. **(a)** Cross-sectional plaque area in distinct parts of the aorta of female *Ldlr*$^{-/-}$ mice after 23 weeks on control or Western diet. Sections were stained by a H/E staining. Scale bars = 100 µm, n = 2–8 aortas of 2–8 mice per group. **(b)** Quantification of the cross-sectional plaque area in distinct segments of the aorta of male and female *Ldlr*$^{-/-}$ mice after 22–25 weeks on control or Western diet. Cross-sectional plaque area was quantified manually. Data are represented as mean ± SEM and were statistically analyzed by a two-way ANOVA test (in case of normal distribution) or by a Kruskal-Wallis test; *p*-values < 0.05 were considered to be significant and indicated by asterisks; **** $p < 0.0001$; n = 2–8 aortas of 2–8 mice per group. Representative images of the experiments are shown [II].

Further experiments showed that *C57BL/6* control mice did not accumulate significant amounts of lipids in the arterial wall, neither on control nor on Western diet (**Figure 18**).

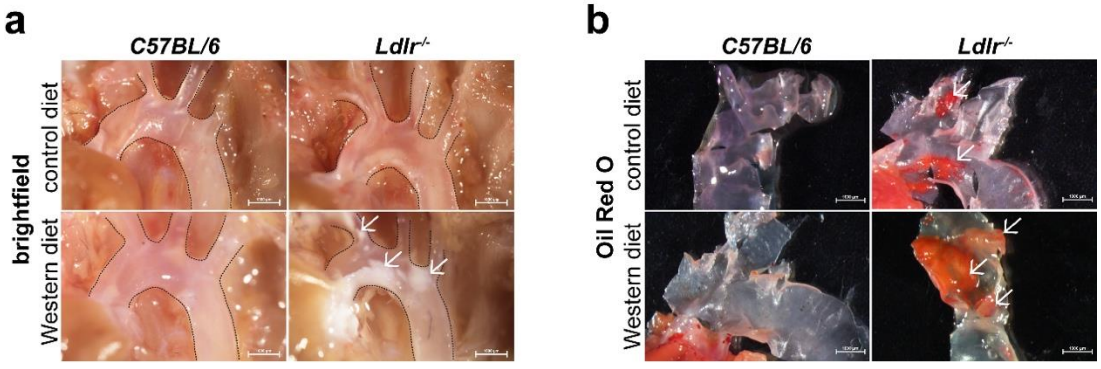

Figure 18: Comparison of plaque development in *C57BL/6* wild-type and *Ldlr*$^{-/-}$ mice. (a) Brightfield images of the aortic arch of female *C57BL/6* and *Ldlr*$^{-/-}$ mice *in situ* after 17 weeks on control or Western diet. Images were acquired by stereo microscopy, scale bar = 1000 µm; n = 3 aortas of 3 mice per group. Arrows indicate plaque formation in the aortic arch. **(b)** Oil Red O staining of whole aortas of female *C57BL/6* and *Ldlr*$^{-/-}$ mice after 17 weeks on control or Western diet. Arrows indicate lipid deposition in the aortic arch. Images were acquired by stereo microscopy, scale bar = 1000 µm; n = 3 aortas of 3 mice per group. Representative images of the experiments are shown [II].

4.2.4 Female Mice on a Western Diet Develop Significantly Larger Plaque Calcifications Than Males

To further assess plaque formation in atherosclerosis, our initial approach was to evaluate the lipid accumulation area within the arterial wall of the aortic arch in male and female *Ldlr*$^{-/-}$ and *ApoE*$^{-/-}$ mice. This was achieved by staining whole aortas with Oil Red O (**Figure 19a**). Analysis of the Oil Red O-positive area indicated a substantial increase in lipid accumulation in the arterial wall of both *Ldlr*$^{-/-}$ and *ApoE*$^{-/-}$ mice fed a Western diet compared to those on a control diet (**Figure 19b**). Interestingly, female *Ldlr*$^{-/-}$ mice exhibited a smaller area of lipid accumulation in the arterial wall compared to males.

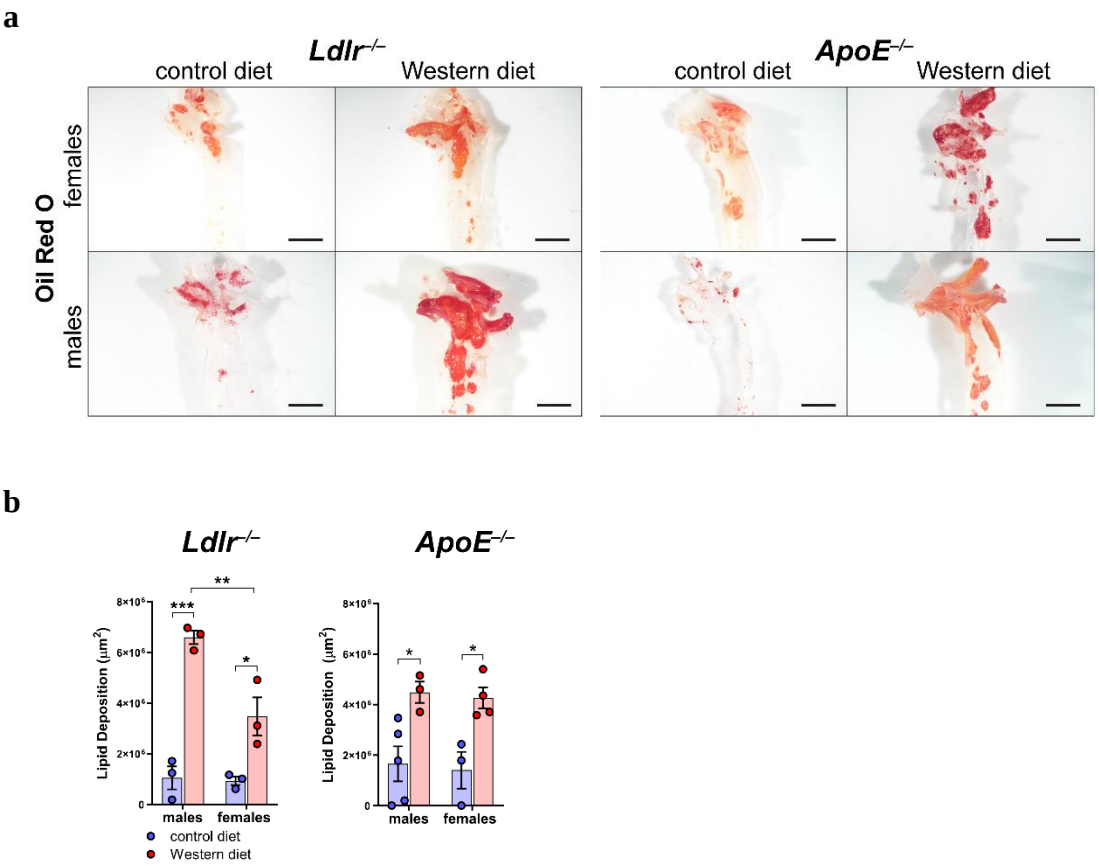

Figure 19: Lipid accumulation in the atherosclerotic plaques of *Ldlr*$^{-/-}$ and *ApoE*$^{-/-}$ mice. (a) Visualization of the lipid deposition in the arterial wall of the aortic arch of *ApoE*$^{-/-}$ and *Ldlr*$^{-/-}$ mice by Oil Red O staining after 18–30 weeks on control or Western diet. Images were acquired by stereo microscopy; scale bar = 2500 µm, n = 3–5 aortas of 3–5 mice per group. **(b)** Quantification of the lipid deposition in the arterial wall of the aortic arch of *Ldlr*$^{-/-}$ and *ApoE*$^{-/-}$ mice after 18–30 weeks on control or Western diet. Oil Red O-positive area was quantified manually. Data are represented as mean ± SEM and were analyzed by a two-way ANOVA test; *p*-values < 0.05 were considered to be significant and indicated by asterisks; * $p < 0.05$; ** $p < 0.01$; *** $p < 0.001$; n = 3–5 aortas of 3–5 mice per group. Representative images of the experiments are shown [II].

To assess plaque fibrosis, we stained cross-sections of the aortic arch of *Ldlr*$^{-/-}$ mice on control and Western diets with Masson Trichrome (Figure not shown). The quantifications showed that the *Ldlr*$^{-/-}$ mice on the Western diet showed a tendency to develop larger cross-sectional fibrotic areas than the animals that had been fed the control diet (Figure not shown). More female mice on the Western diet showed large fibrotic areas of the plaques than the males, suggesting a tendency of females to develop more severe fibrosis of the atherosclerotic plaques. To investigate plaque calcification, we stained whole aortas of male and female *Ldlr*$^{-/-}$ and *ApoE*$^{-/-}$ mice with Alizarin Red S to quantify the calcified plaque area (**Figure 20a**).

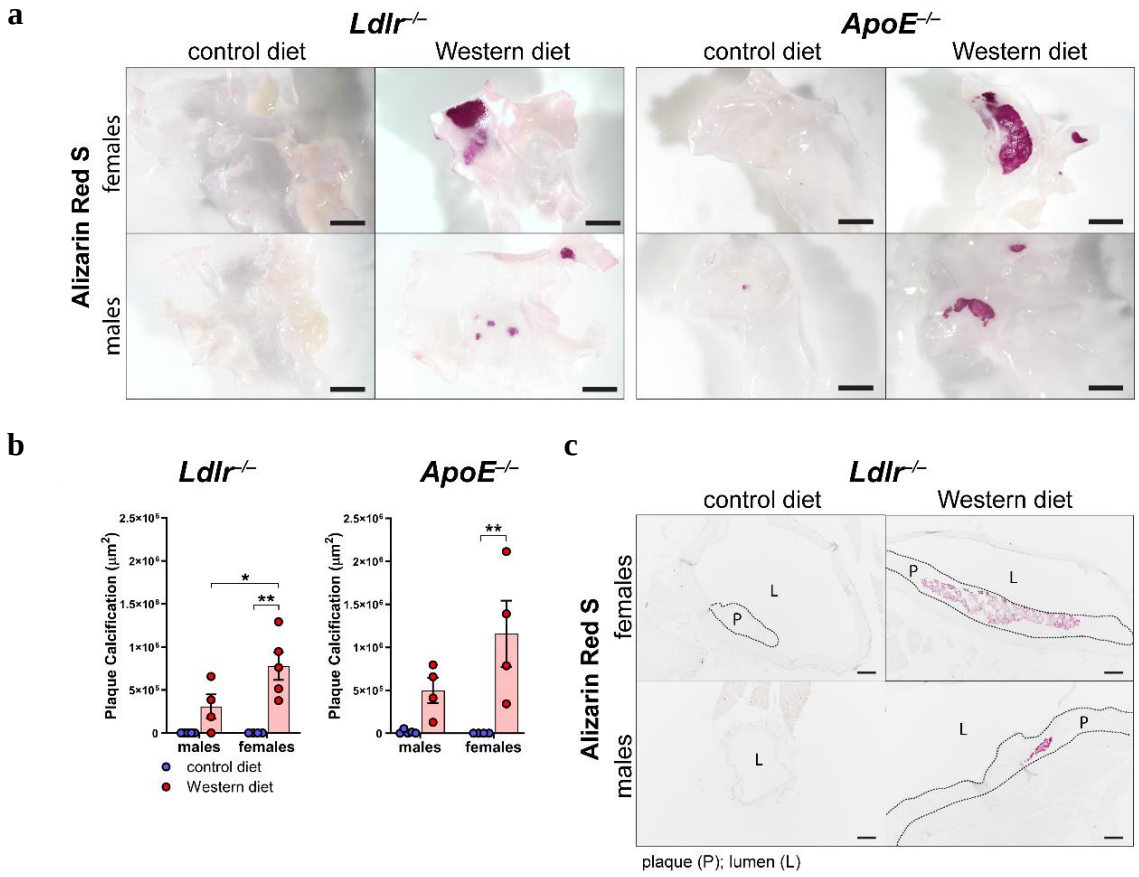

Figure 20. Calcification of the atherosclerotic plaques of *Ldlr*$^{-/-}$ and *ApoE*$^{-/-}$ mice. (a) Visualization of the plaque calcification in the aortic arch of *Ldlr*$^{-/-}$ and *ApoE*$^{-/-}$ mice after 22–26 weeks on control or western diet. Images were acquired by stereo microscopy; scale bar = 2500 µm, n = 4–5 aortas of 4–5 mice per group. Representative images of the experiments are shown. **(b)** Quantification of the calcification of the atherosclerotic plaque of *Ldlr*$^{-/-}$ and *ApoE*$^{-/-}$ mice after 22–26 weeks on control or western diet. Alizarin Red S-positive area was quantified manually. Data are represented as mean ± SEM and were statistically analyzed by a two-way ANOVA test; *p*-values < 0.05 were considered to be significant and were indicated by asterisks; * $p < 0.05$; ** $p < 0.01$; n = 4–5 aortas of 4–5 mice per group. **(c)** Visualization of plaque calcifications in sections of the aortic arch of *Ldlr*$^{-/-}$ and *ApoE*$^{-/-}$ mice after 23–30 weeks on control and western diet. Images were acquired by upright microscopy; scale bars = 100 µm, n = 4–6 aortas of 4–6 mice per group. Representative images of the experiments are shown [II].

Our measurements of the Alizarin Red S-positive regions showed that *Ldlr*$^{-/-}$ and *ApoE*$^{-/-}$ mice on a Western diet experienced significant calcification (**Figure 20b**). Female *Ldlr*$^{-/-}$ mice on this diet developed notably larger calcifications compared to those on a control diet. Additionally, female *Ldlr*$^{-/-}$ mice on the Western diet had a significantly greater calcified area than their male counterparts, indicating a possible influence of sex on plaque calcification. In contrast, male *Ldlr*$^{-/-}$ and *ApoE*$^{-/-}$ mice did not exhibit significant changes in plaque calcification when fed a Western diet. The largest calcified areas were observed in the atherosclerotic plaques of female *Ldlr*$^{-/-}$ and *ApoE*$^{-/-}$ mice on the Western diet. To further examine the differences in plaque calcification, cross-sections of the aortic arch from *Ldlr*$^{-/-}$ mice on both control and Western diets were stained with Alizarin Red S (**Figure 20c**). This staining confirmed that female *Ldlr*$^{-/-}$ mice on the Western diet had larger plaque calcifications.

4.2.5 Lymphatic Count and Total Lymphatic Lumen in Arterial Walls of Atherosclerotic Mice Remain Unchanged

To examine the morphology of the lymphatic vasculature in the arterial walls of male and female *Ldlr*$^{-/-}$ mice on both control and Western diets, we stained cross-sections of various aorta segments using the lymphatic marker anti-LYVE1, as outlined previously [95]. Lymphatic vessels were identified in the thoracic, abdominal, and femoral arteries of *Ldlr*$^{-/-}$ mice on both diets (**Figure 21a**). Similar to earlier findings in wild-type mice, few to no lymphatic vessels were observed in the wall of the aortic arch. The images indicated that lymphatic vessels in the arterial wall maintained a normal appearance without significant morphological changes in mice on the Western diet. Quantification of the lymphatic vessels in the adventitia of different aorta segments in mice on both diets revealed no significant differences in the number of lymphatics, total lymphatic lumen, or average lymphatic lumen (**Figure 21b**). Additionally, no sex-related differences were observed in these lymphatic parameters.

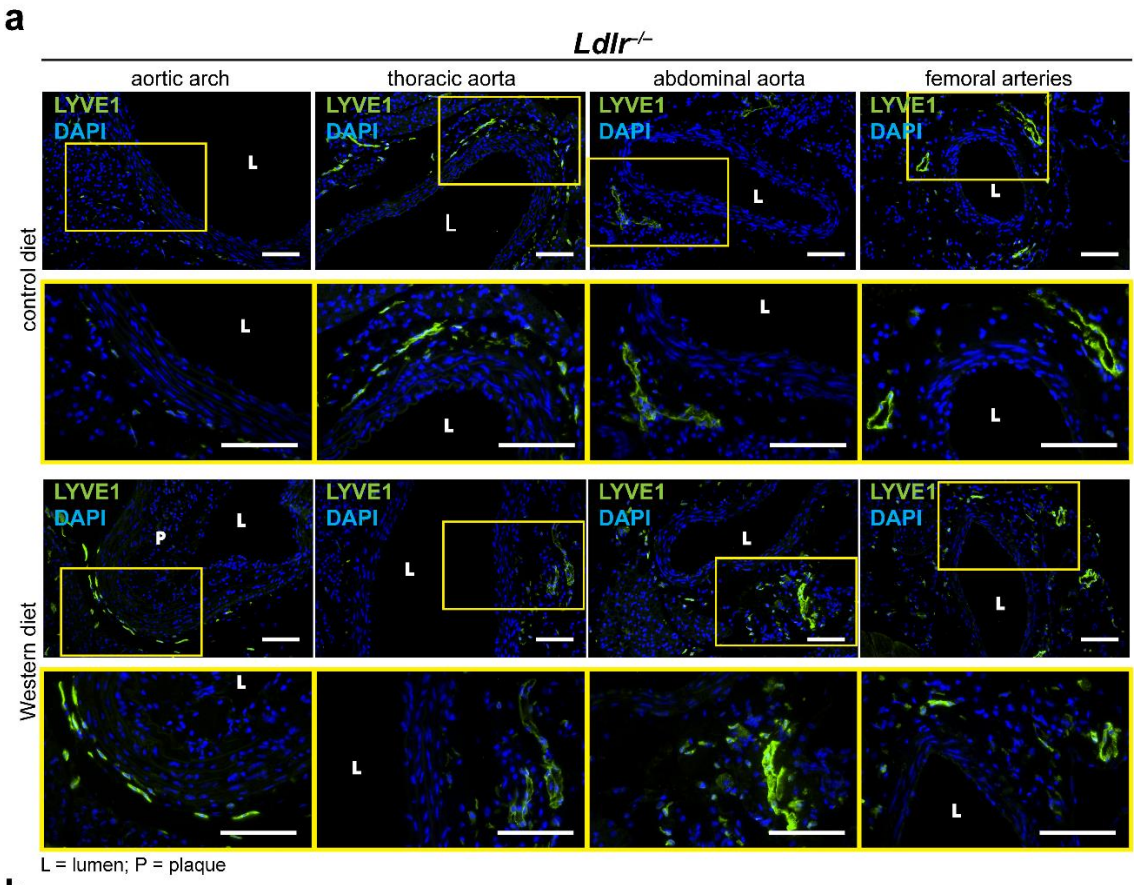
a
Ldlr-/-
aortic arch
thoracic aorta
abdominal aorta
femoral arteries
control diet
Western diet
LYVE1
DAPI
L
P
L = lumen; P = plaque
b
Ldlr-/-
aortic arch
thoracic aorta
abdominal aorta
femoral arteries
control diet
Western diet
Number of Lymphatics
Total Lymphatic Lumen (µm²)
Average Lymphatic Lumen (µm²)
males
females

Figure 21: Lymphatic vessels in the arterial wall of male and female *Ldlr*$^{-/-}$ mice on control or Western diet. (a) Visualization of lymphatic vessels in the adventitia of female *Ldlr*$^{-/-}$ mice after 23–30 weeks on control or Western diet. Sections of distinct parts of the aorta were stained with the lymphatic marker anti-LYVE1. Images were acquired by upright microscopy; scale bars = 100 µm, n = 2–11 aortas of 2–11 mice per group. Representative images of the experiments are shown. **(b)** Quantification of the lymphatic vessels in the adventitia of the aorta of male and female *Ldlr*$^{-/-}$ mice on control or Western diet. Number of lymphatics, total lymphatic lumen and average lymphatic lumen were quantified manually. Data are represented as mean ± SEM and were statistically analyzed by a two-way ANOVA test (in case of normal distribution) or a Kruskal-Wallis test; *p*-values < 0.05 were considered to be significant and indicated by asterisks; * $p < 0.05$; n = 2–11 aortas of 2–11 mice per group [II].

4.2.6 Sex-Dependent Lymphatic Vessel Dilation in the Abdominal Aorta of Female Mice on a Western Diet

To further analyze the lymphatic vasculature in atherosclerosis, we applied tissue-clearing to the aortas of *Ldlr*$^{-/-}$ mice on both control and Western diets, as described in our previous work [95]. The cleared aortas were stained with the lymphatic marker anti-LYVE1 and imaged using stereo microscopy (**Figure 22a**). Quantitative analysis of these images indicated that the Western diet caused a significant, moderate dilation of the lymphatic vessels in the abdominal aorta of female *Ldlr*$^{-/-}$ mice (**Figure 22b**). Conversely, male *Ldlr*$^{-/-}$ mice on the Western diet showed only a slight increase in lymphatic vessel diameter in the abdominal aorta, highlighting a sex-dependent dilation of lymphatic vessels in female mice on a Western diet.

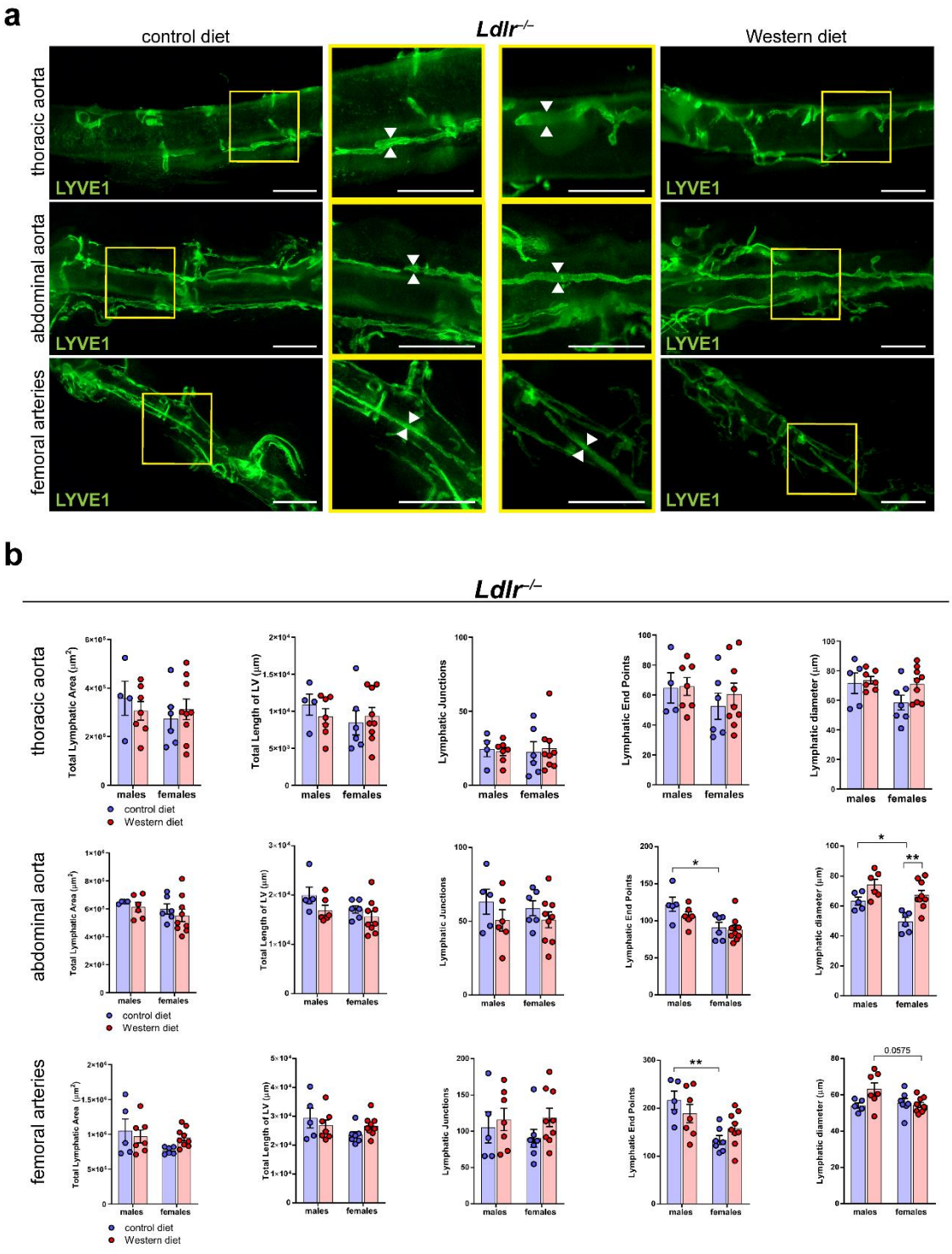
a
control diet
Ldlr-/-
Western diet
thoracic aorta
abdominal aorta
femoral arteries
LYVE1
b
Ldlr-/-
thoracic aorta
abdominal aorta
femoral arteries
Total Lymphatic Area (µm²)
Total Length of LV (µm)
Lymphatic Junctions
Lymphatic End Points
Lymphatic diameter (µm)
males
females
control diet
Western diet
0.0575

Figure 22: Lymphatic vasculature of the tissue-cleared arterial wall of male and female *Ldlr*$^{-/-}$ mice on control or Western diet. (a) Visualization of the lymphatic vasculature of the adventitia of female *Ldlr*$^{-/-}$ mice after 29 weeks on control or Western diet. Aortas were tissue-cleared and stained with the lymphatic marker anti-LYVE1. Images were acquired by stereo microscopy; scale bars = 1000 µm, n = 4–9 aortas of 4–9 mice per group. **(b)** Quantification of the lymphatic vasculature of the aorta of male and female *Ldlr*$^{-/-}$ mice after 21–29 weeks on control or Western diet. Total lymphatic area, total length of lymphatic vessels, lymphatic junctions and lymphatic end points were quantified using AngioTool, lymphatic diameter was manually quantified. Data are represented as mean ± SEM and were statistically analyzed by a two-way ANOVA test (in case of normal distribution) or a Kruskal-Wallis test. *p*-values < 0.05 were considered to be significant and indicated by asterisks; * $p < 0.05$; ** $p < 0.01$; n = 4–9 aortas of 4–9 mice per group. Representative images of the experiments are shown [II].

4.2.7 No Significant Changes in Lymphatic Vessels in Other Organs of *Ldlr*$^{-/-}$ Mice on a Western Diet

To determine if a Western diet affects the lymphatic vasculature in other organs of *Ldlr*$^{-/-}$ mice, we sectioned and stained samples of the small intestines and skin using the lymphatic marker anti-LYVE1 (**Figure 23a** and **c**).

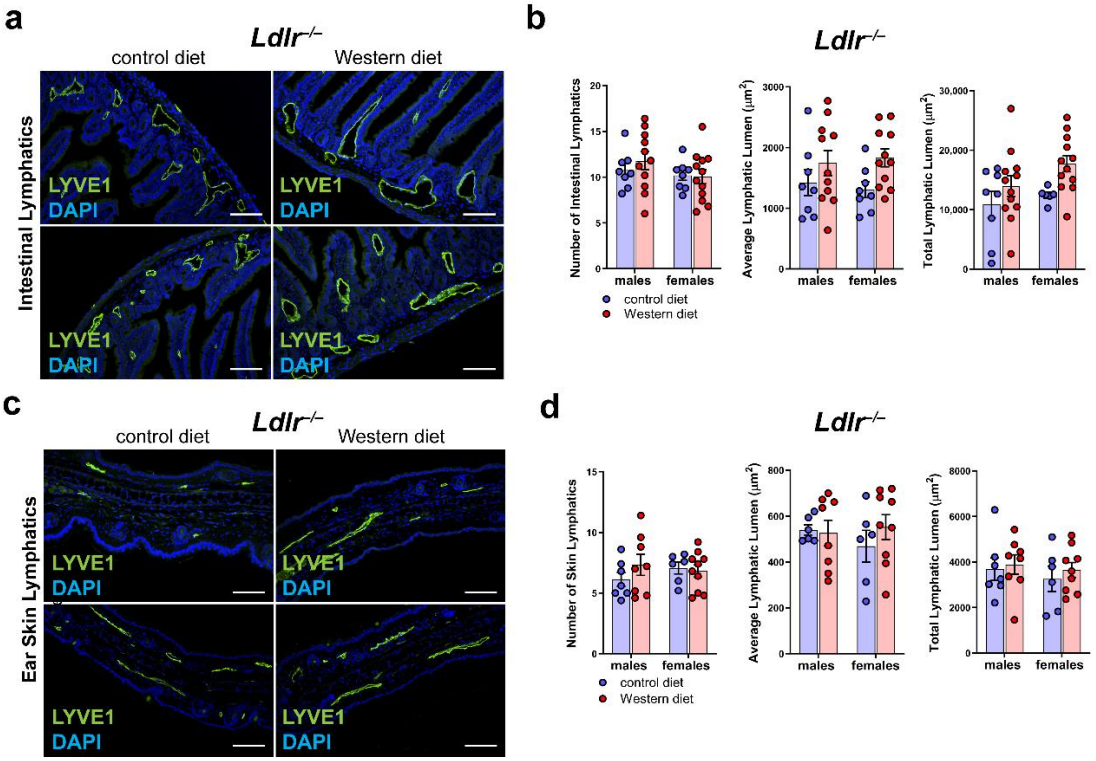

Figure 23. Lymphatic vasculature of the small intestine and the skin in atherosclerosis. (**a**) Visualization of the lymphatic vasculature of small intestine sections of male and female *Ldlr*$^{-/-}$ mice after 22–30 weeks on control or western diet. Sections were stained with the lymphatic marker anti-LYVE1. Images were acquired by upright microscopy; scale bars = 100 µm; n = 8–11 small intestines of 8–11 mice. Representative images of the experiments are shown. (**b**) Quantification of the organ-specific lymphatic vasculature of the small intestine of male and female *Ldlr*$^{-/-}$ mice after 22–30 weeks on control or western diet. Lymphatics were quantified manually. Data were statistically analyzed by a two-way ANOVA test; *p*-values < 0.05 were considered to be significant; n = 8–11 small intestines of 8–11 mice**. (c)** Visualization of the lymphatic vasculature of ear skin sections of male and female *Ldlr*$^{-/-}$ mice after 22–30 weeks on control or western diet. Sections were stained with the lymphatic marker anti-LYVE1. Images were acquired by upright microscopy; scale bars = 100 µm; n = 6–11 ears of 6–11 mice. Representative images of the experiments are shown. (**d**) Quantification of the organ-specific lymphatic vasculature of the skin of male and female *Ldlr*$^{-/-}$ mice after 22–30 weeks on control or Western diet. Lymphatics were quantified manually and statistically analyzed by a two-way ANOVA test. *p* -values < 0.05 were considered to be significant and marked by asterisks; n = 6–11 ears of 6–11 mice [II].

Our analysis of the lymphatic vessels in the intestines of mice on either a control or Western diet showed no difference in the number of lymphatic vessels in the small intestine. There was only a minor, non-significant increase in both the average and total lymphatic lumen in male and female mice on the Western diet (**Figure 23b**). Similarly, in the skin, there was only a slight increase in the lymphatic lumen for mice on the Western diet (**Figure 23d**). No sex-related differences were observed in either the small intestine or the skin.

4.2.8 Enhanced Peripheral Lymphatic Function in Females on a Western Diet

To evaluate peripheral lymphatic function in the hind limbs of *Ldlr*$^{-/-}$ mice on control and Western diets, we injected fluorescently labeled 70kDa Rhodamine Dextran (RhD) into the hind paw and tracked its accumulation in the popliteal lymph nodes (LNs). Initially, we dissected the popliteal LNs to observe any changes in morphology and RhD accumulation (**Figure 24a**). Our analysis revealed that the popliteal LNs in *Ldlr*$^{-/-}$ mice on the Western diet were significantly larger in both males and females, with female mice showing notably larger LNs than their male counterparts (**Figure 24b**). Quantifying the mean intensity of RhD in the popliteal LNs indicated that female *Ldlr*$^{-/-}$ mice on the Western diet had a significantly higher RhD accumulation compared to females on the control diet. Additionally, female *Ldlr*$^{-/-}$ mice on the Western diet tended to accumulate more RhD in the popliteal LNs than their male counterparts, suggesting enhanced peripheral lymphatic function. These findings imply a sex-dependent increase in lymphatic function in female mice on a Western diet.

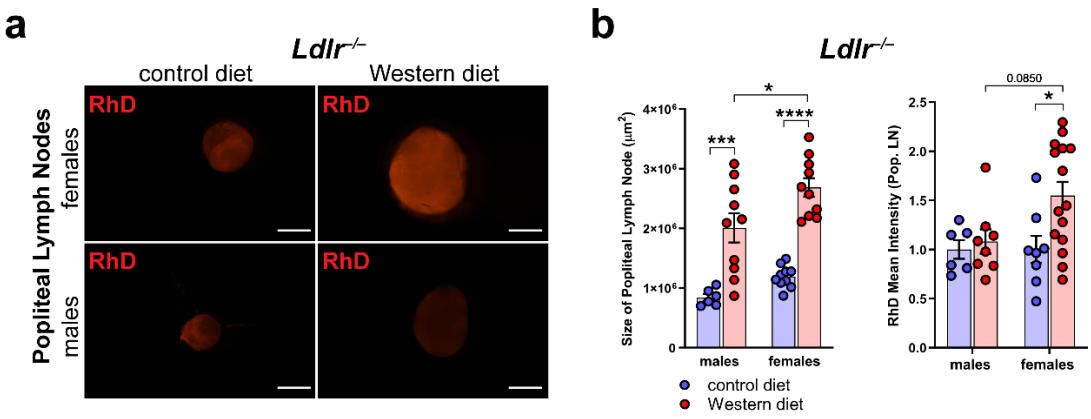

Figure 24: Peripheral lymphatic function in atherosclerosis. **(a)** Visualization of RhD drainage into the popliteal lymph nodes of *Ldlr*$^{-/-}$ mice after 22–30 weeks on control or Western diet. Signal was quantified 90 min after injection of fluorescently labeled 70 kDa RhD into the hind paws; Images were acquired by stereo microscopy; scale bars = 1000 µm; n = 6–12 lymph nodes of 3–6 mice per group. **(b)** Quantification of the size and RhD mean fluorescence intensity of popliteal lymph nodes of *Ldlr*$^{-/-}$ mice after 22–30 weeks on control or Western diet. Data were quantified manually and statistically analyzed by a two-way ANOVA test. *p* -values < 0.05 were considered to be significant; * $p < 0.05$; *** $p < 0.001$; **** $p < 0.0001$; n = 6–12 lymph nodes of 3–6 mice per group [II].

5. Discussion

In this study, we have introduced an effective methodology for visualizing, analyzing, and quantifying the organ-specific growth of lymphatic vessels. Traditional visualization techniques such as paraffin sections, reporter mouse models and whole-mount staining are often insufficient for visualizing lymphatic vasculature due to the opacity of native tissue (**Figure 3 and 4**) [74]. Tissue-clearing techniques offer a solution by rendering tissue samples optically transparent, allowing for imaging. However, many existing protocols have limitations that hinder their suitability for visualizing lymphatic vessels [75,77,78,80,81,85,96-100]. We opted to base our protocol on the non-toxic and efficient CUBIC tissue-clearing protocol [82-84], modifying it to suit our specific needs by adjusting steps, incubation times, and incorporating whole-mount immunostaining to eliminate dependence on reporter mouse models (**Figure 5**).

Our protocol successfully enabled the efficient clearance of various mouse organs without observable tissue shrinkage or damage (**Figure 6**). We demonstrated its compatibility with various fluorescent markers for visualizing organ-specific lymphatic structures (**Figure 7**), as well as its applicability for co-staining with different antibody combinations and investigation of other structures of interest, such as blood vasculature (**Figure 8**). Notably, the fluorescence signals of our samples remained stable for over 18 months, allowing for flexibility in imaging samples and re-imaging after extended periods if needed (**Figure 9**).

Compared to other CUBIC protocols [82-85], we achieved high-quality images using stereo and confocal microscopy without the requirement for expensive and complex light sheet fluorescence microscopy (**Figures 7, 8, 11, 12)**.

Our focus on simplifying analysis led us to quantify our images using AngioTool, a free and user-friendly computational tool specifically designed for vascular structure quantification [94]. AngioTool provided rapid quantification of images with results comparable to manual quantification, making it a suitable tool for assessing lymphatic vasculature (**Figure 10** and **12**).

Subsequently, we utilized our approach to visualize and quantify the organ-specific lymphatic vasculature of *Flt4*$^{kd/+}$ mice, a model exhibiting lymphatic dysfunction symptoms. Although this model was described nearly two decades ago, little is known

about the organ-specific lymphatic vasculature beyond the absence of lymphatics in the skin and dilated intestinal lymphatics [22,89].

Our findings confirmed the absence of lymphatic vessels in the skin and the presence of enlarged lymphatic vessels in the small intestine, as previously reported [22,89]. We identified morphologically altered lymphatic vessels in the lungs, heart, and uterus, which have not been previously described (**Figure 11 and 12**). Additionally, we compared quantifications of tissue-cleared samples with those of tissue sections from the lungs and small intestines of *Flt4*$^{kd/+}$ mice (**Figure 12**). While section-based quantifications provided insights into lymphatic vessels characteristics, tissue-cleared samples enabled more comprehensive assessment, revealing significant reductions in lymphatic junctions, end points, total lymphatic area, and vessel length in *Flt4*$^{kd/+}$ animals. These observations suggest dilated lymphatic vessels and impaired lymphatic function in the lungs and small intestine, highlighting the utility of tissue-cleared samples for accurate organ-specific lymphatic network evaluation.

Our findings regarding morphologically altered organ-specific lymphatic vessels in *Flt4*$^{kd/+}$ mice suggest the significance of lymphatic vessels in maintaining healthy organ function. Further functional studies could elucidate the role of organ-specific lymphatic vessels and the impact of morphologically altered lymphatic vessels on the lymphedema phenotype in *Flt4*$^{kd/+}$ organs.

This study shows that our efficient protocol facilitates the visualization and quantification of lymphatic networks in studied organs, enabling the detection of differences and morphological alterations in lymphatic structures within mouse models. Unlike many tissue-clearing protocols that require expensive equipment and expertise in 3D image analysis, our protocol is accessible to researchers without special equipment or prior knowledge [85].

After developing an efficient approach to visualize lymphatic vessels, we characterized the lymphatic vasculature in atherosclerosis. We unveiled a sex-specific vulnerability to atherosclerosis, with females exhibiting increased development of calcified plaques. While lymphatic vessels within the arterial wall generally remained unchanged in atherosclerosis, notable dilation was observed in the abdominal aorta of female mice on a Western diet. Additionally, these female mice exhibited signs of enhanced peripheral

lymphatic function, indicating potential sex-related alterations in lymphatic function during atherosclerosis.

Previous research has established a connection between lymphatic vessels and atherosclerosis owing to their presence in the arterial wall and their newfound role in reverse cholesterol transport [66-70,101]. However, our comprehension of the extent to which lymphatics contribute to atherosclerosis development and whether sex-dependent differences in lymphatic vasculature has an influence remains limited. While lymphatics have been identified in the adventitia of major vessels, their precise function remains unclear. Although arterial lymphatics are widely believed to be beneficial in atherosclerosis by facilitating the clearance of cholesterol and immune cells from atherosclerotic plaques, recent research has indicated that arterial lymphatics may also contribute to transplant arteriosclerosis, with lymphangiogenesis inhibition potentially preventing transplant arteriosclerosis by suppressing the immune response [71-73,102-104]. Despite investigations of arterial lymphatics in various diseases [30,105], a comprehensive characterization of lymphatic vasculature within the arterial wall has yet to be undertaken. We characterized the lymphatic vasculature of the aorta and identified significant differences in lymphatic network density across the arterial tree. While we were unable to locate lymphatic vessels in the aortic arch, we detected them in the thoracic, abdominal, and femoral segments (**Figure 14**). The majority of lymphatic vessels were concentrated in the abdominal and femoral regions of the aorta. Differences in lymphatic density and its distribution throughout the arterial tree underscore the importance of including distinct aorta segments when investigating the role of lymphatics in vascular disease development and progression.

Moreover, the significance of incorporating distinct aorta segments in studies becomes more apparent when examining plaque formation in atherosclerosis. Our *Ldlr*$^{-/-}$ and *ApoE*$^{-/-}$ mouse models developed the largest atherosclerotic plaques in the brachiocephalic artery and the aortic arch when subjected to a Western diet (**Figure 17, 19** and **20**). Conversely, we could rarely detect plaques in the femoral arteries and only sporadically in the abdominal aorta. Site-specific susceptibility to plaque formation in the aortic arch is attributed to hemodynamic forces, such as low shear stress and oscillatory or turbulent blood flow affecting the endothelium, often occurring in areas of branching or high vessel curvature [106]. The absence of lymphatic vessels in the aortic arch where

the largest atherosclerotic plaques were localized in our study might suggest a potential lymphatic contribution to site-specific plaque development.

Both *Ldlr*$^{-/-}$ and *ApoE*$^{-/-}$ mice exhibited elevated serum lipids, primarily driven by increased LDL levels (**Figure 17**). These findings were consistent with previously published studies on *Ldlr*$^{-/-}$ and *ApoE*$^{-/-}$ mouse models [56-58,60,90]. In accordance to previous studies, *C57BL/6* control mice did not develop atherosclerotic plaques when fed a Western diet, supporting the notion that the loss of LDLR and resultant hyperlipidemia are major contributors to atherosclerosis development (**Figure 18**) [58].

We observed a tendency for female *Ldlr*$^{-/-}$ mice to develop larger atherosclerotic plaques in the aortic arch compared to males (**Figure 17**), along with significantly larger calcifications (**Figure 20**). In advanced atherosclerosis, smooth muscle cells or macrophages in the arterial wall undergo apoptosis and release matrix vesicles, leading to vascular calcification [53]. Calcification typically manifests in advanced atherosclerosis and serves as an indicator of disease severity. These findings align with recent analyses of previously published atherosclerosis studies, which suggested that female mice tend to develop larger atherosclerotic lesions than males [107-109]. In contrast, human epidemiological data indicate that young women under 60 years of age are less susceptible to cardiovascular disease than men but surpass them by the age of 80 [48,110]. These sex-specific differences in atherosclerosis development, observed in both humans and animals, underscore the importance of including both sexes in disease research to avoid biased results that could influence the effectiveness of future treatments.

Numerous studies have highlighted alterations in lymphatic vessels in atherosclerosis. It has been demonstrated that the number and size of lymphatic vessels increase in atherosclerosis, with lymphatic function impacting plaque size [71,73]. In our study, we did not observe differences in the number or size of lymphatics in the arterial wall of atherosclerotic mice, nor did we detect significant morphological changes in the lymphatic vasculature (**Figure 21**). However, examination of tissue-cleared aortas from female *Ldlr*$^{-/-}$ mice on a Western diet revealed dilated lymphatic vessels in the arterial wall of the abdominal aorta (**Figure 22**). Moderate dilation of lymphatic vessels may indicate altered lymphatic function in the arterial wall, potentially involved in excess cholesterol removal via increased reverse cholesterol transport (RCT). Additionally, we observed slightly dilated lymphatic vessels in the small intestine and skin of mice on the

Western diet. These findings align with those of Lim *et al*., who suggested that lymphatic vessels play a crucial role in RCT, with moderate dilation in the small intestine and skin possibly indicating increased RCT to remove excess cholesterol from these organs (**Figure 23**) [66].

Monitoring lymphatic function in the arterial wall poses significant challenges; thus, we assessed peripheral lymphatic function in the hind limbs of atherosclerotic mice (**Figure 24**). Lymph drainage from the hind limbs of female *Ldlr*$^{-/-}$ mice on the Western diet was significantly elevated, resulting in a higher accumulation of RhD in the popliteal LNs. Moreover, we observed significant enlargement of popliteal LNs in female mice on the Western diet, indicative of an inflammatory process in these animals. These findings parallel those of a study by Shin *et al*., which demonstrated higher expression of inflammation- and apoptosis-associated genes in the endothelial cells of female atherosclerotic mice compared to males [111]. These results suggest a sex-dependent alteration in lymphatic function in atherosclerosis, the precise role of which remains unclear and underscores the necessity for further investigation of lymphatic function in atherosclerosis.

One of the challenges in studying lymphatics in atherosclerosis is the difficulty in monitoring lymphatic function within large vessels in vivo or in situ. Our approach involved visualizing peripheral lymphatic function in atherosclerotic mice to explore the impact of a Western diet on atherosclerosis. However, a more comprehensive understanding of lymphatic function within large vessels would be advantageous. Given the extended duration of atherosclerosis studies, spanning several months, it was impractical to incorporate diverse time points and include both *ApoE*$^{-/-}$ and *Ldlr*$^{-/-}$ mice in each individual experiment. To further advance our understanding of the role of lymphatic function in atherosclerosis development, exploring other atherosclerosis models such as rabbits or larger animal models, and ideally human subjects, would be beneficial.

In this study, we have demonstrated that lymphatic vessels exhibit non-uniform distribution throughout the arterial tree, potentially influencing site-specific susceptibility to plaque formation in atherosclerosis. Our experiments indicated that lymphatic vessel morphology remains largely unchanged in atherosclerosis. Existing literature on the role of lymphatics in atherosclerosis presents varying findings, highlighting the need for

further research to comprehensively understand their role in different aspects of atherosclerosis [70,73,101,102,112,113]. The observation that female mice develop more severe manifestations of atherosclerosis, including increased calcification alongside enlarged lymph nodes and heightened peripheral lymphatic function, suggests the existence of a potential sex-dependent compensatory mechanism mediated by lymphatics that could impact reverse cholesterol transport (RCT) and immune cell transportation. This insight opens avenues for further exploration into the intricate interplay between lymphatic function, sex-specific differences, and atherosclerosis progression, suggesting promising directions for future investigations in this field.

6. Conclusion

In this study we characterized and quantified organ-specific lymphatic growth with a focus on sex-dependent differences in atherosclerosis, utilizing an optimized tissue-clearing protocol.

- Our optimized tissue-clearing technique provides a straightforward method to visualizing and quantifying organ-specific lymphatic growth, all without the need for specialized equipment, software, or prior expertise, thus making tissue-clearing available for researchers of all backgrounds.
- Our technique enables the visualization and quantification of morphological alterations in the lymphatic vasculature, making it an efficient tool to visualize and quantify lymphatic disorders.
- In our investigation, we observed dilated and diminished lymphatic structures in the lungs, uterus, and heart of *Flt4*$^{kd/+}$ mice, expanding upon previous findings limited to the skin.
- Throughout our investigation, we found that lymphatic vessels are distributed unevenly within the arterial tree, with sparse presence in the aortic arch and abundance in abdominal and femoral arteries.
- In our study, we observed that female mice tend to develop larger plaques with significantly larger calcifications compared to males.
- We also noted that the lymphatic vasculature of large vessels remains mostly unaffected by atherosclerosis, except for dilation in the abdominal aorta of female mice on a Western diet.
- Furthermore, mice on a Western diet exhibited enlarged popliteal lymph nodes, particularly pronounced in females.
- Lastly, females demonstrated increased peripheral lymphatic function compared to males on a Western diet.

7. Summary

Organ-specific lymphatics play a crucial role in maintaining tissue homeostasis and influencing the development of various diseases. However, understanding their precise functions has been challenging due to limitations in visualization techniques. This study presents a novel approach to overcoming these challenges, providing new insights into lymphatic function across different organs. with a focus on the great vessels.

The objectives of this study were to develop and validate a visualization technique to achieve efficient and detailed visualization of lymphatic structures across various mouse organs. Additionally, we aimed to investigate the role of lymphatic vessels in atherosclerosis, with a focus on sex-specific differences.

We employed a modified CUBIC tissue-clearing protocol coupled with whole-mount immunostaining to visualize lymphatic structures in mouse organs. This method was applied to *Flt4*$^{kd/+}$ mice, a model for lymphedema, as well as to *ApoE*$^{-/-}$ and *LDLR*$^{-/-}$ mice, mouse models for atherosclerosis. Quantification of lymphatic networks was performed using AngioTool, a software tool for the assessment of vascular structures.

Our method successfully enabled high-quality imaging of lymphatic structures across various mouse organs without the need for specialized equipment, offering a cost-effective alternative for researchers. Application of the technique to *Flt4*$^{kd/+}$ mice revealed significant morphological alterations in lymphatic structures across multiple organs. In the context of atherosclerosis, we found that lymphatic vessels were unevenly distributed within the arterial tree, with sparse presence in the aortic arch and abundance in the abdominal and femoral arteries. Additionally, female mice on Western diet developed larger plaques with more significant calcifications than male mice and enhanced peripheral lymphatic function, suggesting sex-specific factors in plaque formation and lymphatic function during atherosclerosis.

Our findings underscore the critical role of organ-specific lymphatics in both health and disease. The novel tissue-clearing and visualization technique developed in this study provides a powerful tool for researchers to explore lymphatic function and its involvement in disease pathogenesis. The observed sex-specific differences in plaque formation and lymphatic function in atherosclerosis highlight the need for further research into lymphatic involvement in disease and the potential for therapeutic interventions targeting these pathways.

8. References

1. Loukas, M.; Bellary, S.S.; Kuklinski, M.; Ferrauiola, J.; Yadav, A.; Shoja, M.M.; Shaffer, K.; Tubbs, R.S. The lymphatic system: a historical perspective. *Clin Anat* **2011**, *24*, 807-816, doi:10.1002/ca.21194.
2. Alitalo, K.; Carmeliet, P. Molecular mechanisms of lymphangiogenesis in health and disease. *Cancer Cell* **2002**, *1*, 219-227, doi:10.1016/s1535-6108(02)00051-x.
3. Baluk, P.; Fuxe, J.; Hashizume, H.; Romano, T.; Lashnits, E.; Butz, S.; Vestweber, D.; Corada, M.; Molendini, C.; Dejana, E.; McDonald DM. Functionally specialized junctions between endothelial cells of lymphatic vessels. *J Exp Med* **2007**, *204*, 2349-2362, doi:10.1084/jem.20062596.
4. Levick, J.R.; Michel, C.C. Microvascular fluid exchange and the revised Starling principle. *Cardiovasc Res* **2010**, *87*, 198-210, doi:10.1093/cvr/cvq062.
5. Solari, E.; Marcozzi, C.; Negrini, D.; Moriondo, A. Lymphatic Vessels and Their Surroundings: How Local Physical Factors Affect Lymph Flow. *Biology (Basel)* **2020**, *9*, doi:10.3390/biology9120463.
6. Srinivasan, R.S.; Oliver, G. Prox1 dosage controls the number of lymphatic endothelial cell progenitors and the formation of the lymphovenous valves. *Genes Dev* **2011**, *25*, 2187-2197, doi:10.1101/gad.16974811.
7. Janardhan, H.P.; Trivedi, C.M. Establishment and maintenance of blood-lymph separation. *Cell Mol Life Sci* **2019**, *76*, 1865-1876, doi:10.1007/s00018-019-03042-3.
8. Wigle, J.T.; Harvey, N.; Detmar, M.; Lagutina, I.; Grosveld, G.; Gunn, M.D.; Jackson, D.G.; Oliver, G. An essential role for Prox1 in the induction of the lymphatic endothelial cell phenotype. *EMBO J* **2002**, *21*, 1505-1513, doi:10.1093/emboj/21.7.1505.
9. Wigle, J.T.; Oliver, G. Prox1 function is required for the development of the murine lymphatic system. *Cell* **1999**, *98*, 769-778, doi:10.1016/s0092-8674(00)81511-1.
10. Oliver, G.; Sosa-Pineda, B.; Geisendorf, S.; Spana, E.P.; Doe, C.Q.; Gruss, P. Prox 1, a prospero-related homeobox gene expressed during mouse development. *Mech Dev* **1993**, *44*, 3-16, doi:10.1016/0925-4773(93)90012-m.

11. Hong, Y.K.; Harvey, N.; Noh, Y.H.; Schacht, V.; Hirakawa, S.; Detmar, M.; Oliver, G. Prox1 is a master control gene in the program specifying lymphatic endothelial cell fate. *Dev Dyn* **2002**, *225*, 351-357, doi:10.1002/dvdy.10163.

12. Semo, J.; Nicenboim, J.; Yaniv, K. Development of the lymphatic system: new questions and paradigms. *Development* **2016**, *143*, 924-935, doi:10.1242/dev.132431.

13. Hagerling, R.; Pollmann, C.; Andreas, M.; Schmidt, C.; Nurmi, H.; Adams, R.H.; Alitalo, K.; Andresen, V.; Schulte-Merker, S.; Kiefer, F. A novel multistep mechanism for initial lymphangiogenesis in mouse embryos based on ultramicroscopy. *EMBO J* **2013**, *32*, 629-644, doi:10.1038/emboj.2012.340.

14. Sabin, F.R. On the origin of the lymphatic system from the veins and the development of the lymph hearts and thoracic duct in the pig. *American Journal of Anatomy* **1902**.

15. Kaipainen, A.; Korhonen, J.; Mustonen, T.; van Hinsbergh, V.W.; Fang, G.H.; Dumont, D.; Breitman, M.; Alitalo, K. Expression of the fms-like tyrosine kinase 4 gene becomes restricted to lymphatic endothelium during development. *Proc Natl Acad Sci U S A* **1995**, *92*, 3566-3570, doi:10.1073/pnas.92.8.3566.

16. Joukov, V.; Pajusola, K.; Kaipainen, A.; Chilov, D.; Lahtinen, I.; Kukk, E.; Saksela, O.; Kalkkinen, N.; Alitalo, K. A novel vascular endothelial growth factor, VEGF-C, is a ligand for the Flt4 (VEGFR-3) and KDR (VEGFR-2) receptor tyrosine kinases. *The EMBO Journal* **1996**, *15*, 290-298, doi:10.1002/j.1460-2075.1996.tb00359.x.

17. Bos, F.L.; Caunt, M.; Peterson-Maduro, J.; Planas-Paz, L.; Kowalski, J.; Karpanen, T.; van Impel, A.; Tong, R.; Ernst, J.A.; Korving, J.; van Es JH, Lammert E, Duckers HJ, Schulte-Merker S. CCBE1 is essential for mammalian lymphatic vascular development and enhances the lymphangiogenic effect of vascular endothelial growth factor-C in vivo. *Circ Res* **2011**, *109*, 486-491, doi:10.1161/CIRCRESAHA.111.250738.

18. Jeltsch, M.; Jha, S.K.; Tvorogov, D.; Anisimov, A.; Leppanen, V.M.; Holopainen, T.; Kivela, R.; Ortega, S.; Karpanen, T.; Alitalo, K. CCBE1 enhances lymphangiogenesis via A disintegrin and metalloprotease with thrombospondin motifs-3-mediated vascular endothelial growth factor-C activation. *Circulation* **2014**, *129*, 1962-1971, doi:10.1161/CIRCULATIONAHA.113.002779.

19. Le Guen, L.; Karpanen, T.; Schulte, D.; Harris, N.C.; Koltowska, K.; Roukens, G.; Bower, N.I.; van Impel, A.; Stacker, S.A.; Achen, M.G.; Schulte-Merker S., Hogan BM. Ccbe1 regulates Vegfc-mediated induction of Vegfr3 signaling during embryonic lymphangiogenesis. *Development* **2014**, *141*, 1239-1249, doi:10.1242/dev.100495.

20. Brouillard, P.; Boon, L.; Vikkula, M. Genetics of lymphatic anomalies. *J Clin Invest* **2014**, *124*, 898-904, doi:10.1172/JCI71614.

21. Mendola, A.; Schlogel, M.J.; Ghalamkarpour, A.; Irrthum, A.; Nguyen, H.L.; Fastre, E.; Bygum, A.; van der Vleuten, C.; Fagerberg, C.; Baselga, E.; Quere I., Mulliken JB., Boon LM., Brouillard P., Vikkula M. Mutations in the VEGFR3 signaling pathway explain 36% of familial lymphedema. *Mol Syndromol* **2013**, *4*, 257-266, doi:10.1159/000354097.

22. Karkkainen, M.J.; Saaristo, A.; Jussila, L.; Karila, K.A.; Lawrence, E.C.; Pajusola, K.; Bueler, H.; Eichmann, A.; Kauppinen, R.; Kettunen, M.I.; Yla-Herttuala S., Finegold DN., Ferrell RE., Alitalo K. A model for gene therapy of human hereditary lymphedema. *Proc Natl Acad Sci U S A* **2001**, *98*, 12677-12682, doi:10.1073/pnas.221449198.

23. Suneale Banerji; Jian Ni; Shu-Xia Wang; Steven Clasper; Jeffrey Su; Raija Tammi; Margaret Jones; Jackson, D.G. Lyve 1 a new homologue of the cd44 glycoprotein is a lymph specific receptor for hyaluronan. *The Journal of Cell Biology* **1999**, *144*, 789Ð801.

24. Wu, M.; Du, Y.; Liu, Y.; He, Y.; Yang, C.; Wang, W.; Gao, F. Low molecular weight hyaluronan induces lymphangiogenesis through LYVE-1-mediated signaling pathways. *PLoS One* **2014**, *9*, e92857, doi:10.1371/journal.pone.0092857.

25. G. Ostgaard, R.R. Intravenous saline infusion in rat increases hyaluronan efflux in intestinal lymph by increasing lymph flow. *Acta. Physiol. Scand.* **1993**, 329–335.

26. Gale, N.W.; Prevo, R.; Espinosa, J.; Ferguson, D.J.; Dominguez, M.G.; Yancopoulos, G.D.; Thurston, G.; Jackson, D.G. Normal lymphatic development and function in mice deficient for the lymphatic hyaluronan receptor LYVE-1. *Mol Cell Biol* **2007**, *27*, 595-604, doi:10.1128/MCB.01503-06.

27. Huang, S.S.; Liu, I.H.; Smith, T.; Shah, M.R.; Johnson, F.E.; Huang, J.S. CRSBP-1/LYVE-l-null mice exhibit identifiable morphological and functional alterations of lymphatic capillary vessels. *FEBS Lett* **2006**, *580*, 6259-6268, doi:10.1016/j.febslet.2006.10.028.

28. C. Mouta Carreira, S.N., E. di Tomaso, T. Padera, Y. Boucher, S. Tomarev, R. Jain. LYVE-1 is not restricted to the lymph vessels: expression in normal liver blood sinusoids and down-regulation in human liver cancer and cirrhosis. *Cancer Res.* **2001**, *61*, 8079-8084.

29. Adamczyk, L.A.; Gordon, K.; Kholova, I.; Meijer-Jorna, L.B.; Telinius, N.; Gallagher, P.J.; van der Wal, A.C.; Baandrup, U. Lymph vessels: the forgotten second circulation in health and disease. *Virchows Arch* **2016**, *469*, 3-17, doi:10.1007/s00428-016-1945-6.

30. Oliver, G.; Kipnis, J.; Randolph, G.J.; Harvey, N.L. The Lymphatic Vasculature in the 21(st) Century: Novel Functional Roles in Homeostasis and Disease. *Cell* **2020**, *182*, 270-296, doi:10.1016/j.cell.2020.06.039.

31. Escobedo, N.; Proulx, S.T.; Karaman, S.; Dillard, M.E.; Johnson, N.; Detmar, M.; Oliver, G. Restoration of lymphatic function rescues obesity in Prox1-haploinsufficient mice. *JCI Insight* **2016**, *1*, doi:10.1172/jci.insight.85096.

32. Harvey, N.L.; Srinivasan, R.S.; Dillard, M.E.; Johnson, N.C.; Witte, M.H.; Boyd, K.; Sleeman, M.W.; Oliver, G. Lymphatic vascular defects promoted by Prox1 haploinsufficiency cause adult-onset obesity. *Nat Genet* **2005**, *37*, 1072-1081, doi:10.1038/ng1642.

33. Carlson, J.A. Lymphedema and subclinical lymphostasis (microlymphedema) facilitate cutaneous infection, inflammatory dermatoses, and neoplasia: A locus minoris resistentiae. *Clin Dermatol* **2014**, *32*, 599-615, doi:10.1016/j.clindermatol.2014.04.007.

34. Pena-Jimenez, D.; Fontenete, S.; Megias, D.; Fustero-Torre, C.; Grana-Castro, O.; Castellana, D.; Loewe, R.; Perez-Moreno, M. Lymphatic vessels interact dynamically with the hair follicle stem cell niche during skin regeneration in vivo. *EMBO J* **2019**, *38*, e101688, doi:10.15252/embj.2019101688.

35. von der Weid, P.Y.; Rehal, S.; Ferraz, J.G. Role of the lymphatic system in the pathogenesis of Crohn's disease. *Curr Opin Gastroenterol* **2011**, *27*, 335-341, doi:10.1097/MOG.0b013e3283476e8f.

36. D'Alessio, S.; Correale, C.; Tacconi, C.; Gandelli, A.; Pietrogrande, G.; Vetrano, S.; Genua, M.; Arena, V.; Spinelli, A.; Peyrin-Biroulet, L.; Fiocchi C., Danese S. VEGF-C-dependent stimulation of lymphatic function ameliorates experimental inflammatory bowel disease. *J Clin Invest* **2014**, *124*, 3863-3878, doi:10.1172/JCI72189.

37. Davis, R.B.; Kechele, D.O.; Blakeney, E.S.; Pawlak, J.B.; Caron, K.M. Lymphatic deletion of calcitonin receptor-like receptor exacerbates intestinal inflammation. *JCI Insight* **2017**, *2*, e92465, doi:10.1172/jci.insight.92465.

38. Summers, B.D.; Kim, K.; Clement, C.C.; Khan, Z.; Thangaswamy, S.; McCright, J.; Maisel, K.; Zamora, S.; Quintero, S.; Racanelli, A.C.; Redmond D., D'Armiento J., Yang J., Kuang A., Monticelli L., Kahn ML., Choi AMK., Santambrogio L., Reed HO. Lung lymphatic thrombosis and dysfunction caused by cigarette smoke exposure precedes emphysema in mice. *Sci Rep* **2022**, *12*, 5012, doi:10.1038/s41598-022-08617-y.

39. Jakus, Z.; Gleghorn, J.P.; Enis, D.R.; Sen, A.; Chia, S.; Liu, X.; Rawnsley, D.R.; Yang, Y.; Hess, P.R.; Zou, Z.; Yang J., Guttentag SH., Nelson CM., Kahn ML. Lymphatic function is required prenatally for lung inflation at birth. *J Exp Med* **2014**, *211*, 815-826, doi:10.1084/jem.20132308.

40. Szotak-Ajtay, K.; Szoke, D.; Kovacs, G.; Andreka, J.; Brenner, G.B.; Giricz, Z.; Penninger, J.; Kahn, M.L.; Jakus, Z. Reduced Prenatal Pulmonary Lymphatic Function Is Observed in Clp1 (K/K) Embryos With Impaired Motor Functions Including Fetal Breathing Movements in Preparation of the Developing Lung for Inflation at Birth. *Front Bioeng Biotechnol* **2020**, *8*, 136, doi:10.3389/fbioe.2020.00136.

41. Varricchi, G.; Granata, F.; Loffredo, S.; Genovese, A.; Marone, G. Angiogenesis and lymphangiogenesis in inflammatory skin disorders. *J Am Acad Dermatol* **2015**, *73*, 144-153, doi:10.1016/j.jaad.2015.03.041.

42. Shi, V.Y.; Bao, L.; Chan, L.S. Inflammation-driven dermal lymphangiogenesis in atopic dermatitis is associated with CD11b+ macrophage recruitment and VEGF-C up-regulation in the IL-4-transgenic mouse model. *Microcirculation* **2012**, *19*, 567-579, doi:10.1111/j.1549-8719.2012.00189.x.

43. Xu, H.; Edwards, J.; Banerji, S.; Prevo, R.; Jackson, D.G.; Athanasou, N.A. Distribution of lymphatic vessels in normal and arthritic human synovial tissues. *Ann Rheum Dis* **2003**, *62*, 1227-1229, doi:10.1136/ard.2003.005876.

44. Alexander, J.S.; Chaitanya, G.V.; Grisham, M.B.; Boktor, M. Emerging roles of lymphatics in inflammatory bowel disease. *Ann N Y Acad Sci* **2010**, *1207 Suppl 1*, E75-85, doi:10.1111/j.1749-6632.2010.05757.x.

45. Herrington, W.; Lacey, B.; Sherliker, P.; Armitage, J.; Lewington, S. Epidemiology of Atherosclerosis and the Potential to Reduce the Global Burden of Atherothrombotic Disease. *Circ Res* **2016**, *118*, 535-546, doi:10.1161/CIRCRESAHA.115.307611.

46. Song, P.; Fang, Z.; Wang, H.; Cai, Y.; Rahimi, K.; Zhu, Y.; Fowkes, F.G.R.; Fowkes, F.J.I.; Rudan, I. Global and regional prevalence, burden, and risk factors for carotid atherosclerosis: a systematic review, meta-analysis, and modelling study. *Lancet Glob Health* **2020**, *8*, e721-e729, doi:10.1016/S2214-109X(20)30117-0.

47. Virani, S.S.; Alonso, A.; Benjamin, E.J.; Bittencourt, M.S.; Callaway, C.W.; Carson, A.P.; Chamberlain, A.M.; Chang, A.R.; Cheng, S.; Delling, F.N.; Djousse L, Elkind MSV, Ferguson JF, Fornage M, Khan SS, Kissela BM, Knutson KL, Kwan TW, Lackland DT, Lewis TT, Lichtman JH, Longenecker CT, Loop MS, Lutsey PL, Martin SS, Matsushita K, Moran AE, Mussolino ME, Perak AM, Rosamond WD, Roth GA, Sampson UKA, Satou GM, Schroeder EB, Shah SH, Shay CM., Spartano NL., Stokes A., Tirschwell DL., VanWagner LB., Tsao CW. Heart Disease and Stroke Statistics-2020 Update: A Report From the American Heart Association. *Circulation* **2020**, *141*, e139-e596, doi:10.1161/CIR.0000000000000757.

48. Tsao, C.W.; Aday, A.W.; Almarzooq, Z.I.; Alonso, A.; Beaton, A.Z.; Bittencourt, M.S.; Boehme, A.K.; Buxton, A.E.; Carson, A.P.; Commodore-Mensah, Y.; Elkind MSV, Evenson KR, Eze-Nliam C, Ferguson JF, Generoso G, Ho JE, Kalani R, Khan SS, Kissela BM, Knutson KL, Levine DA, Lewis TT, Liu J, Loop MS, Ma J, Mussolino ME, Navaneethan SD, Perak AM, Poudel R, Rezk-Hanna M, Roth GA, Schroeder EB, Shah SH, Thacker EL, VanWagner LB, Virani SS, Voecks JH, Wang NY, Yaffe K, Martin SS. Heart Disease and Stroke Statistics-2022 Update: A Report From the American Heart Association. *Circulation* **2022**, *145*, e153-e639, doi:10.1161/CIR.0000000000001052.

49. Nakashima, Y.; Raines, E.W.; Plump, A.S.; Breslow, J.L.; Ross, R. Upregulation of VCAM-1 and ICAM-1 at atherosclerosis-prone sites on the endothelium in the ApoE-deficient mouse. *Arterioscler Thromb Vasc Biol* **1998**, *18*, 842-851, doi:10.1161/01.atv.18.5.842.

50. Kzhyshkowska, J.; Neyen, C.; Gordon, S. Role of macrophage scavenger receptors in atherosclerosis. *Immunobiology* **2012**, *217*, 492-502, doi:10.1016/j.imbio.2012.02.015.

51. Moore, K.J.; Freeman, M.W. Scavenger receptors in atherosclerosis: beyond lipid uptake. *Arterioscler Thromb Vasc Biol* **2006**, *26*, 1702-1711, doi:10.1161/01.ATV.0000229218.97976.43.

52. Boullier, A.; Bird, D.A.; Chang, M.K.; Dennis, E.A.; Friedman, P.; Gillotre-Taylor, K.; Horkko, S.; Palinski, W.; Quehenberger, O.; Shaw, P.; Steinberg D, Terpstra V, Witztum JL. Scavenger receptors, oxidized LDL, and atherosclerosis. *Ann N Y Acad Sci* **2001**, *947*, 214-222; discussion 222-213, doi:10.1111/j.1749-6632.2001.tb03943.x.

53. New, S.E.; Goettsch, C.; Aikawa, M.; Marchini, J.F.; Shibasaki, M.; Yabusaki, K.; Libby, P.; Shanahan, C.M.; Croce, K.; Aikawa, E. Macrophage-derived matrix vesicles: an alternative novel mechanism for microcalcification in atherosclerotic plaques. *Circ Res* **2013**, *113*, 72-77, doi:10.1161/CIRCRESAHA.113.301036.

54. Wenk, J.F. Numerical Modeling of Stress in Stenotic Arteries With Microcalcifications: A Parameter Sensitivity Study. *Journal of Biomechanical Engineering* **2010**, *133*, doi:10.1115/1.4003128.

55. Thomas, H.; Diamond, J.; Vieco, A.; Chaudhuri, S.; Shinnar, E.; Cromer, S.; Perel, P.; Mensah, G.A.; Narula, J.; Johnson, C.O.; Roth GA, Moran AE. Global Atlas of Cardiovascular Disease 2000-2016: The Path to Prevention and Control. *Glob Heart* **2018**, *13*, 143-163, doi:10.1016/j.gheart.2018.09.511.

56. Reddick, R.L.; Zhang, S.H.; Maeda, N. Atherosclerosis in Mice Lacking Apo E. Evaluation of Lesional Development and Progression. *Arterioscler Thromb Vasc Biol* **1994**, *14*, 141-147, doi:10.1161/01.ATV.14.1.141.

57. Meir, K.S.; Leitersdorf, E. Atherosclerosis in the apolipoprotein-E-deficient mouse: a decade of progress. *Arterioscler Thromb Vasc Biol* **2004**, *24*, 1006-1014, doi:10.1161/01.ATV.0000128849.12617.f4.

58. Awan, Z.; Denis, M.; Bailey, D.; Giaid, A.; Prat, A.; Goltzman, D.; Seidah, N.G.; Genest, J. The LDLR deficient mouse as a model for aortic calcification and quantification by micro-computed tomography. *Atherosclerosis* **2011**, *219*, 455-462, doi:10.1016/j.atherosclerosis.2011.08.035.

59. Ishibashi, S.; Brown, M.S.; Goldstein, J.L.; Gerard, R.D.; Hammer, R.E.; Herz, J. Hypercholesterolemia in low density lipoprotein receptor knockout mice and its reversal by adenovirus-mediated gene delivery. *J Clin Invest* **1993**, *92*, 883-893, doi:10.1172/JCI116663.

60. Getz, G.; Reardon, C. Animal Models of Atherosclerosis. *Arterioscler Thromb Vasc Biol* **2012**, *32*, 1104-1115, doi:10.1161/ATVBAHA.111.237693.

61. Knowles, J.; Maeda, N. Genetic Modifiers of Atherosclerosis in Mice. *Arterioscler Thromb Vasc Biol* **2000**, *20*, 2336-2345, doi:10.1161/01.atv.20.11.2336.

62. Plump AS; Smith JD; Hayek T; Aalto-Setälä K; Walsh A; Verstuyft JG; Rubin EM; JL, B. Severe hypercholesterolemia and atherosclerosis in apolipoprotein e deficient mice created by homologous recombination in es cells. *Cell* **1992**, doi:10.1016/0092-8674(92)90362-g.

63. Ishibashi, S.; Goldstein, J.L.; Brown, M.S.; Herz, J.; Burns, D.K. Massive xanthomatosis and atherosclerosis in cholesterol-fed low density lipoprotein receptor-negative mice. *J Clin Invest* **1994**, *93*, 1885-1893, doi:10.1172/JCI117179.

64. Nakashima, Y.; Plump, A.S.; Raines, E.W.; Breslow, J.L.; Ross, R. ApoE-Deficient Mice Develop Lesions of All Phases of Atherosclerosis Throughout the Arterial Tree. *Arterioscler Thromb Vasc Biol* **1994**, *14*, 133-140, doi:10.1161/01.atv.14.1.133.

65. Erin M. Foley, J.D.E. Hepatic Heparan Sulfate Proteoglycans and Endocytic Clearance of Triglyceride-Rich Lipoproteins. *Progress in Molecular Biology and Translational Science* **2010**, *93*, 213-233.

66. Lim, H.Y.; Thiam, C.H.; Yeo, K.P.; Bisoendial, R.; Hii, C.S.; McGrath, K.C.; Tan, K.W.; Heather, A.; Alexander, J.S.; Angeli, V. Lymphatic vessels are essential for the removal of cholesterol from peripheral tissues by SR-BI-mediated transport of HDL. *Cell Metab* **2013**, *17*, 671-684, doi:10.1016/j.cmet.2013.04.002.

67. Martel, C.; Li, W.; Fulp, B.; Platt, A.M.; Gautier, E.L.; Westerterp, M.; Bittman, R.; Tall, A.R.; Chen, S.H.; Thomas, M.J.; Kreisel D, Swartz MA, Sorci-Thomas MG, Randolph GJ. Lymphatic vasculature mediates macrophage reverse cholesterol transport in mice. *J Clin Invest* **2013**, *123*, 1571-1579, doi:10.1172/JCI63685.

68. Hoggan, G.; Hoggan, F.E. The Lymphatics of the Walls of the Larger Blood Vessels and Lymphatics. *J Anat Physiol.* **1882**, *17*, 1-23.

69. Johnson, R.A. Lymphatics of Blood Vessels. *Lymphology* **1969**, *2*, 44-56.

70. Drozdz, K.; Janczak, D.; Dziegiel, P.; Podhorska, M.; Patrzalek, D.; Ziolkowski, P.; Andrzejak, R.; Szuba, A. Adventitial lymphatics of internal carotid artery in healthy and atherosclerotic vessels. *Folia Histochem Cytobiol* **2008**, *46*, 433-436, doi:10.2478/v10042-008-0083-7.

71. Rademakers, T.; van der Vorst, E.P.; Daissormont, I.T.; Otten, J.J.; Theodorou, K.; Theelen, T.L.; Gijbels, M.; Anisimov, A.; Nurmi, H.; Lindeman, J.H.; Schober A, Heeneman S, Alitalo K, Biessen EA. Adventitial lymphatic capillary expansion impacts on plaque T cell accumulation in atherosclerosis. *Sci Rep* **2017**, *7*, 45263, doi:10.1038/srep45263.

72. Vuorio, T.; Nurmi, H.; Moulton, K.; Kurkipuro, J.; Robciuc, M.R.; Ohman, M.; Heinonen, S.E.; Samaranayake, H.; Heikura, T.; Alitalo, K.; Ylä-Herttuala S. Lymphatic vessel insufficiency in hypercholesterolemic mice alters lipoprotein levels and promotes atherogenesis. *Arterioscler Thromb Vasc Biol* **2014**, *34*, 1162-1170, doi:10.1161/ATVBAHA.114.302528.

73. Milasan, A.; Smaani, A.; Martel, C. Early rescue of lymphatic function limits atherosclerosis progression in Ldlr(-/-) mice. *Atherosclerosis* **2019**, *283*, 106-119, doi:10.1016/j.atherosclerosis.2019.01.031.

74. Jacques, S.L. Optical properties of biological tissues: A review. *Phys. Med. Biol.* **2013**, *58*, R37-R61.

75. Chi, J.; Crane, A.; Wu, Z.; Cohen, P. Adipo-Clear: A Tissue Clearing Method for Three-Dimensional Imaging of Adipose Tissue. *J Vis Exp* **2018**, doi:10.3791/58271.

76. Kellner, M.; Heidrich, M.; Lorbeer, R.A.; Antonopoulos, G.C.; Knudsen, L.; Wrede, C.; Izykowski, N.; Grothausmann, R.; Jonigk, D.; Ochs, M.; Ripken T.; Kühnel M.; Meyer H. A combined method for correlative 3D imaging of biological samples from macro to nano scale. *Sci Rep* **2016**, *6*, 35606, doi:10.1038/srep35606.

77. Perbellini, F.; Liu, A.K.L.; Watson, S.A.; Bardi, I.; Rothery, S.M.; Terracciano, C.M. Free-of-Acrylamide SDS-based Tissue Clearing (FASTClear) for three dimensional visualization of myocardial tissue. *Sci Rep* **2017**, *7*, 5188, doi:10.1038/s41598-017-05406-w.

78. Renier, N.; Wu, Z.; Simon, D.J.; Yang, J.; Ariel, P.; Tessier-Lavigne, M. iDISCO: a simple, rapid method to immunolabel large tissue samples for volume imaging. *Cell* **2014**, *159*, 896-910, doi:10.1016/j.cell.2014.10.010.

79. Zhan, Y.; Wu, H.; Liu, L.; Lin, J.; Zhang, S. Organic solvent-based tissue clearing techniques and their applications. *J Biophotonics* **2021**, *14*, e202000413, doi:10.1002/jbio.202000413.

80. Tomer, R.; Ye, L.; Hsueh, B.; Deisseroth, K. Advanced CLARITY for rapid and high-resolution imaging of intact tissues. *Nat Protoc* **2014**, *9*, 1682-1697, doi:10.1038/nprot.2014.123.

81. Oren, R.; Fellus-Alyagor, L.; Addadi, Y.; Bochner, F.; Gutman, H.; Blumenreich, S.; Dafni, H.; Dekel, N.; Neeman, M.; Lazar, S. Whole Organ Blood and Lymphatic Vessels Imaging (WOBLI). *Sci Rep* **2018**, *8*, 1412, doi:10.1038/s41598-018-19663-w.

82. Susaki, E.A.; Tainaka, K.; Perrin, D.; Kishino, F.; Tawara, T.; Watanabe, T.M.; Yokoyama, C.; Onoe, H.; Eguchi, M.; Yamaguchi, S.; Abe T, Kiyonari H, Shimizu Y, Miyawaki A, Yokota H, Ueda HR. Whole-brain imaging with single-cell resolution using chemical cocktails and computational analysis. *Cell* **2014**, *157*, 726-739, doi:10.1016/j.cell.2014.03.042.

83. Susaki, E.A.; Tainaka, K.; Perrin, D.; Yukinaga, H.; Kuno, A.; Ueda, H.R. Advanced CUBIC protocols for whole-brain and whole-body clearing and imaging. *Nat Protoc* **2015**, *10*, 1709-1727, doi:10.1038/nprot.2015.085.

84. Tainaka, K.; Kubota, S.I.; Suyama, T.Q.; Susaki, E.A.; Perrin, D.; Ukai-Tadenuma, M.; Ukai, H.; Ueda, H.R. Whole-body imaging with single-cell resolution by tissue decolorization. *Cell* **2014**, *159*, 911-924, doi:10.1016/j.cell.2014.10.034.

85. Takahashi, K.; Abe, K.; Kubota, S.I.; Fukatsu, N.; Morishita, Y.; Yoshimatsu, Y.; Hirakawa, S.; Kubota, Y.; Watabe, T.; Ehata, S.; Ueda HR, Shimamura T, Miyazono K. An analysis modality for vascular structures combining tissue-clearing technology and topological data analysis. *Nat Commun* **2022**, *13*, 5239, doi:10.1038/s41467-022-32848-2.

86. Xu, Y.; He, Q.; Wang, M.; Wu, Y.; Shi, Y.; Wang, W.; Zhang, J. Three-dimensional visualization of human brain tumors using the CUBIC technique. *Brain Tumor Pathol* **2023**, *40*, 4-14, doi:10.1007/s10014-022-00445-2.

87. Mano, T.; Murata, K.; Kon, K.; Shimizu, C.; Ono, H.; Shi, S.; Yamada, R.G.; Miyamichi, K.; Susaki, E.A.; Touhara, K.; Ueda HR. CUBIC-Cloud provides an integrative computational framework toward community-driven whole-mouse-brain mapping. *Cell Rep Methods* **2021**, *1*, 100038, doi:10.1016/j.crmeth.2021.100038.

88. Choi, I.; Chung, H.K.; Ramu, S.; Lee, H.N.; Kim, K.E.; Lee, S.; Yoo, J.; Choi, D.; Lee, Y.S.; Aguilar, B.; Hong YK. Visualization of lymphatic vessels by Prox1-promoter

directed GFP reporter in a bacterial artificial chromosome-based transgenic mouse. *Blood* **2011**, *117*, 362-365, doi:10.1182/blood-2010-07-298562.

89. Karkkainen, M.J.; Saaristo, A.; Jussila, L.; Karila, K.A.; Lawrence, E.C.; Pajusola, K.; Bueler, H.; Eichmann, A.; Kauppinen, R.; Kettunen, M.I.; Yla-Herttuala S, Finegold DN, Ferrell RE, Alitalo K. A model for gene therapy of human hereditary lymphedema. *Proceedings of the National Academy of Sciences* **2001**, *98*, 12677-12682, doi:10.1073/pnas.221449198.

90. Piedrahita, J.A.Z., S.H.; Hagaman, J.R.; Oliver, P.M.; Maeda, N. Generation of mice carrying a mutant apolipoprotein E gene inactivated by gene targeting in embryonic stem cells. *Proc. Natl. Acad. Sci. USA* **1992**, *89*, 4471-4475, doi:10.1073/pnas.89.10.4471.

91. Szoke, D.; Kovacs, G.; Kemecsei, E.; Balint, L.; Szotak-Ajtay, K.; Aradi, P.; Styevkone Dinnyes, A.; Mui, B.L.; Tam, Y.K.; Madden, T.D.; Karikó K, Kataru RP, Hope MJ, Weissman D, Mehrara BJ, Pardi N, Jakus Z. Nucleoside-modified VEGFC mRNA induces organ-specific lymphatic growth and reverses experimental lymphedema. *Nat Commun* **2021**, *12*, 3460, doi:10.1038/s41467-021-23546-6.

92. Kauffenstein, G.; Pizard, A.; Le Corre, Y.; Vessieres, E.; Grimaud, L.; Toutain, B.; Labat, C.; Mauras, Y.; Gorgels, T.G.; Bergen, A.A.; Le Saux O, Lacolley P, Lefthériotis G, Henrion D, Martin L. Disseminated arterial calcification and enhanced myogenic response are associated with abcc6 deficiency in a mouse model of pseudoxanthoma elasticum. *Arterioscler Thromb Vasc Biol* **2014**, *34*, 1045-1056, doi:10.1161/ATVBAHA.113.302943.

93. Schindelin, J.; Arganda-Carreras, I.; Frise, E.; Kaynig, V.; Longair, M.; Pietzsch, T.; Preibisch, S.; Rueden, C.; Saalfeld, S.; Schmid, B.; Tinevez JY, White DJ, Hartenstein V, Eliceiri K, Tomancak P, Cardona A. Fiji: an open-source platform for biological-image analysis. *Nat Methods* **2012**, *9*, 676-682, doi:10.1038/nmeth.2019.

94. Zudaire, E.; Gambardella, L.; Kurcz, C.; Vermeren, S. A computational tool for quantitative analysis of vascular networks. *PLoS One* **2011**, *6*, e27385, doi:10.1371/journal.pone.0027385.

95. Christ, C.; Jakus, Z. Visualization of Organ-Specific Lymphatic Growth: An Efficient Approach to Labeling Molecular Markers in Cleared Tissues. *Int J Mol Sci* **2023**, *24*, doi:10.3390/ijms24065075.

96. Gomez-Gaviro, M.V.; Balaban, E.; Bocancea, D.; Lorrio, M.T.; Pompeiano, M.; Desco, M.; Ripoll, J.; Vaquero, J.J. Optimized CUBIC protocol for three-dimensional imaging of chicken embryos at single-cell resolution. *Development* **2017**, *144*, 2092-2097, doi:10.1242/dev.145805.

97. Ke, M.T.; Fujimoto, S.; Imai, T. SeeDB: a simple and morphology-preserving optical clearing agent for neuronal circuit reconstruction. *Nat Neurosci* **2013**, *16*, 1154-1161, doi:10.1038/nn.3447.

98. Kuwajima, T.; Sitko, A.A.; Bhansali, P.; Jurgens, C.; Guido, W.; Mason, C. ClearT: a detergent- and solvent-free clearing method for neuronal and non-neuronal tissue. *Development* **2013**, *140*, 1364-1368, doi:10.1242/dev.091844.

99. Nehrhoff, I.; Bocancea, D.; Vaquero, J.; Vaquero, J.J.; Ripoll, J.; Desco, M.; Gomez-Gaviro, M.V. 3D imaging in CUBIC-cleared mouse heart tissue: going deeper. *Biomed Opt Express* **2016**, *7*, 3716-3720, doi:10.1364/BOE.7.003716.

100. Susaki, E.A.; Ueda, H.R. Whole-body and Whole-Organ Clearing and Imaging Techniques with Single-Cell Resolution: Toward Organism-Level Systems Biology in Mammals. *Cell Chem Biol* **2016**, *23*, 137-157, doi:10.1016/j.chembiol.2015.11.009.

101. Csanyi, G.; Singla, B. Arterial Lymphatics in Atherosclerosis: Old Questions, New Insights, and Remaining Challenges. *J Clin Med* **2019**, *8*, doi:10.3390/jcm8040495.

102. Kutkut, I.; Meens, M.J.; McKee, T.A.; Bochaton-Piallat, M.L.; Kwak, B.R. Lymphatic vessels: an emerging actor in atherosclerotic plaque development. *Eur J Clin Invest* **2015**, *45*, 100-108, doi:10.1111/eci.12372.

103. Yeo, K.P.L., H.J.; Thiam, C.H.; Azhar, S.H.; Tan, C.; Tang, Y.; See, W.Q.; Koh, X.H.; Zhao, M.H.; Phua, M.L.; Balachander, A.; Tan, Y.; Lim, S.Y; Chew, H.S.; Ng, L.G.; Angeli, V. Efficient aortic lymphatic drainage is necessary for atherosclerosis regression induced by ezetimibe. *Sci. Adv.* **2020**, *6*, doi:DOI: 10.1126/sciadv.abc2697.

104. Chen, K.; Mou, R.; Zhu, P.; Xu, X.; Wang, H.; Jiang, L.; Hu, Y.; Hu, X.; Ma, L.; Xiao, Q.; Xu Q. The Effect of Lymphangiogenesis in Transplant Arteriosclerosis. *Circulation* **2023**, *147*, 482-497, doi:10.1161/CIRCULATIONAHA.122.060799.

105. Yeo, K.P.; Lim, H.Y.; Angeli, V. Leukocyte Trafficking via Lymphatic Vessels in Atherosclerosis. *Cells* **2021**, *10*, doi:10.3390/cells10061344.

106. VanderLaan, P.A.; Reardon, C.A.; Getz, G.S. Site specificity of atherosclerosis: site-selective responses to atherosclerotic modulators. *Arterioscler Thromb Vasc Biol* **2004**, *24*, 12-22, doi:10.1161/01.ATV.0000105054.43931.f0.

107. Man, J.J.; Beckman, J.A.; Jaffe, I.Z. Sex as a Biological Variable in Atherosclerosis. *Circ Res* **2020**, *126*, 1297-1319, doi:10.1161/CIRCRESAHA.120.315930.

108. Mansukhani, N.A.; Wang, Z.; Shively, V.P.; Kelly, M.E.; Vercammen, J.M.; Kibbe, M.R. Sex Differences in the LDL Receptor Knockout Mouse Model of Atherosclerosis. *Artery Res* **2017**, *20*, 8-11, doi:10.1016/j.artres.2017.08.002.

109. Robinet, P.; Milewicz, D.M.; Cassis, L.A.; Leeper, N.J.; Lu, H.S.; Smith, J.D. Consideration of Sex Differences in Design and Reporting of Experimental Arterial Pathology Studies-Statement From ATVB Council. *Arterioscler Thromb Vasc Biol* **2018**, *38*, 292-303, doi:10.1161/ATVBAHA.117.309524.

110. Lloyd-Jones, D.; Adams, R.; Carnethon, M.; De Simone, G.; Ferguson, T.B.; Flegal, K.; Ford, E.; Furie, K.; Go, A.; Greenlund, K.; Haase N, Hailpern S, Ho M, Howard V, Kissela B, Kittner S, Lackland D, Lisabeth L, Marelli A, McDermott M, Meigs J, Mozaffarian D, Nichol G, O'Donnell C, Roger V, Rosamond W, Sacco R, Sorlie P, Stafford R, Steinberger J, Thom T, Wasserthiel-Smoller S, Wong N, Wylie-Rosett J, Hong Y. Heart disease and stroke statistics--2009 update: a report from the American Heart Association Statistics Committee and Stroke Statistics Subcommittee. *Circulation* **2009**, *119*, e21-181, doi:10.1161/CIRCULATIONAHA.108.191261.

111. Shin, J.; Hong, J.; Edwards-Glenn, J.; Krukovets, I.; Tkachenko, S.; Adelus, M.L.; Romanoski, C.E.; Rajagopalan, S.; Podrez, E.; Byzova, T.V.; Stenina-Adongravi O, Cherepanova OA. Unraveling the Role of Sex in Endothelial Cell Dysfunction: Evidence From Lineage Tracing Mice and Cultured Cells. *Arterioscler Thromb Vasc Biol* **2024**, *44*, 238-253, doi:10.1161/ATVBAHA.123.319833.

112. Xu, X.; Lin, H.; Lv, H.; Zhang, M.; Zhang, Y. Adventitial lymphatic vessels -- an important role in atherosclerosis. *Med Hypotheses* **2007**, *69*, 1238-1241, doi:10.1016/j.mehy.2007.04.007.

113. Nakano, T.; Nakashima, Y.; Yonemitsu, Y.; Sumiyoshi, S.; Chen, Y.X.; Akishima, Y.; Ishii, T.; Iida, M.; Sueishi, K. Angiogenesis and lymphangiogenesis and

expression of lymphangiogenic factors in the atherosclerotic intima of human coronary arteries. *Hum Pathol* **2005**, *36*, 330-340, doi:10.1016/j.humpath.2005.01.001.

9. Bibliography of the candidate's publications

9.1 Publications included in this dissertation

I Christ C, Jakus Z.
Visualization of Organ-Specific Lymphatic Growth: An Efficient Approach to Labeling Molecular Markers in Cleared Tissues. Int J Mol Sci. 2023 Mar 7;24(6):5075. doi: 10.3390/ijms24065075. PMID: 36982150.
Impact Factor: 5.6

II Christ C, Ocskay Z, Kovács G, Jakus Z.
Characterization of Atherosclerotic Mice Reveals a Sex-Dependent Susceptibility to Plaque Calcification but No Major Changes in the Lymphatics in the Arterial Wall. Int J Mol Sci. 2024 Apr 5;25(7):4046. doi: 10.3390/ijms25074046. PMID: 38612867.
Impact Factor: 5.6

9.2 Publications not included in this dissertation

III Ocskay Z, Bálint L, **Christ C**, Kahn ML, Jakus Z.
CCBE1 regulates the development and prevents the age-dependent regression of meningeal lymphatics. Biomed Pharmacother. 2024 Jan;170:116032. doi: 10.1016/j.biopha.2023.116032. PMID: 38141283.
Impact Factor: 7.5

IV Tauber P, Aichinger B, **Christ C**, Stindl J, Rhayem Y, Beuschlein F, Warth R, Bandulik S. Cellular Pathophysiology of an Adrenal Adenoma-Associated Mutant of the Plasma Membrane Ca(2+)-ATPase ATP2B3. Endocrinology. 2016 Jun;157(6):2489-99. doi: 10.1210/en.2015-2029. PMID: 27035656.
Impact Factor: 4.9

10. Acknowledgments

First and foremost, I would like to express my gratitude to my supervisor, Dr. Zoltán Jakus. His guidance over the past years has been invaluable. Dr. Jakus has been not only a great supervisor but also a mentor whose support has profoundly shaped my academic journey.

I want to thank Semmelweis University and Prof. Hunyady and Prof. Mócsai who were leading the Physiology Department during my time there. They created, together with the Head of the Doctoral School, Prof. Ligeti, a great environment and team spirit that I truly enjoyed and benefited from immensely.

Special thanks to my outstanding colleagues Éva Kemecsei, Zsombor Ocskay, Gábor Kovács, Petra Aradi, Kitti Ajtai and Valéria Németh who worked with me side by side for all those years and who have made the most challenging days manageable. I want to especially thank Éva Kemecsei, who also became my dear friend, for her support and friendship throughout these years.

Thanks to the amazing team in the animal facility, Eszter and Ádám Marinkás and Dorisz Csengel, who helped us with the animal maintenance.

My family, especially my parents, your belief in me and constant support have been essential. From the very beginning, you have stood by me through both the good times and the bad. I could not have reached this milestone without you. Thank you!

My partner Jamie, your patience and understanding as I navigated through the long journey to completing my PhD have been incredible. You stood beside me through it all, believing in me when I needed it most. This has meant so much to me!

Lastly, I would like to thank everyone involved in reviewing my thesis, including the reviewers and the members of the committee. Your insights and feedback have been instrumental in refining this work.

Thank you all for your contributions, support, and encouragement.

Funding:

This work was supported by the National Research, Development, and Innovation Office (K139165, TKP2021-EGA-29, TKP2021-EGA-24, NVKP_16-1-2016-0039), the European Union, and the Hungarian Government (VEKOP-2.3.2-16-2016-00002, VEKOP-2.3.3-15-2016-00006, EFOP-3.6.3-VEKOP-16-2017-00009). Z.J. is a recipient of the János Bolyai Research Scholarship of the Hungarian Academy of Sciences (BO/00898/22) and the New National Excellence Program of the Ministry for Culture and Innovation from the source of the National Research, Development, and Innovation Fund (UNKP-23-5-SE-10).